# Direct evidence of the formation mechanisms of TiC nanoparticles and Al<sub>3</sub>Ti intermetallics during synthesis of an Al/TiC metal matrix nanocomposite

Aaron Gladstein<sup>a,\*</sup>, Shanmukha Kiran Aramanda<sup>a,\*</sup>, Lingxia Shi<sup>a</sup>, Jason Landini<sup>a</sup>, Jonathan Goettsch<sup>a</sup>, Caleb Reese<sup>b</sup>, Bibhu Sahu<sup>a</sup>, Xianghui Xiao<sup>c</sup>, Allen Hunter<sup>d</sup>, Katsuyo Thornton<sup>a</sup>, Ashwin J. Shahani<sup>a,e,\*\*</sup>, Alan I. Taub<sup>a,f,\*\*</sup>

<sup>a</sup>Department of Materials Science and Engineering, University of Michigan, Ann Arbor, MI 48109, USA
 <sup>b</sup>General Motors Research & Development, Detroit, MI 48092, USA
 <sup>c</sup>National Synchrotron Light Source II, Brookhaven National Laboratory, Upton, NY 11973, USA
 <sup>d</sup>Michigan Center for Materials Characterization, University of Michigan, Ann Arbor, MI 48109, USA
 <sup>e</sup>Department of Chemical Engineering, University of Michigan, Ann Arbor, MI 48109, USA
 <sup>f</sup>Department of Mechanical Engineering, University of Michigan, Ann Arbor, MI 48109, USA

#### Abstract

Microstructure control of in situ metal matrix nanocomposites (MMNCs) poses a barrier to their large-scale production. Here, we interrogate in unprecedented detail the formation mechanisms, morphologies, and microstructures of an in situ Al/TiC MMNC processed via salt flux reaction. Through synchrotron-based X-ray nanotomography (TXM) and scanning and transmission electron microscopy, we visualize in over five orders-of-magnitude of length-scale the TiC nanoparticles, Al<sub>3</sub>Ti intermetallics, and their co-locations. 3D reconstructions from TXM revealed a surprising variety of Al<sub>3</sub>Ti morphologies, including an orthogonal plate structure. By combining our experimental results with phase-field simulations, we demonstrate that this growth form originates from the intermetallic nucleating epitaxially on a TiC particle which is larger than a critical size at a given undercooling. Yet TiC particles that are too small to nucleate Al<sub>3</sub>Ti can also impact the growth of the intermetallic, by splitting the intermetallic plates during solidification. These insights on the divalent roles of the nanoparticles offer general guidelines for the synthesis and processing of MMNCs.

Keywords: Metal matrix nanocomposites; heterogeneous nucleation; intermetallics; nanoparticles; advanced characterization; synchrotron radiation; X-ray nanotomography.

#### 1. Introduction

Current demands for fuel-efficiency and increased electric vehicle range in the automotive and aerospace industries continue to push the necessity for strong and lightweight materials. Al alloys have been used extensively due to their high strength-to-weight ratio, but the reduction of mechanical properties at elevated temperatures limits their application. In comparison to base alloys, Al-based metal matrix nanocomposites

Email addresses: shahani@umich.edu (Ashwin J. Shahani), alantaub@umich.edu (Alan I. Taub)

<sup>\*</sup>These authors contributed equally to the work.

<sup>\*\*</sup>Corresponding authors

(MMNCs) have improved mechanical properties at both ambient and elevated temperatures, which depend on the reinforcement characteristics (e.g., size, volume fraction, and morphology of nanoparticles) [1], [2], [3], [4], [5], [6], [7], [8], [9], [10], [11], [12], [13]. TiC is particularly attractive as a reinforcement phase because of its high hardness and elastic modulus, low density, and low chemical reactivity [14]. Such Al/TiC MMNCs are often produced through ex situ methods, where the reinforcement particles are premade and mixed into the matrix [3], [5], [6], [8], [12], thereby allowing for control over particle size, type, and volume fraction. However, these ex situ processing methods can lead to reinforcement contamination [4], [15], undesirable particle-matrix interfacial reactions [15], [16], and poor particle-matrix wetting [4], [17], thus hindering production of large-scale MMNCs.

Alternatively, in situ methods generate reinforcing particles directly in the melt via reactive processes, thereby avoiding some of the difficulties mentioned above [2, 14, 12, 18, 19, 20, 21]. The reactions to form particles in situ are typically complex and can involve intermediate reaction steps, parallel reaction pathways that result in different reinforcement morphologies, and the generation of undesirable secondary phases, including intermetallics, all of which influence the final microstructure and mechanical properties [19, 20, 22, 23, 24, 25, 26, 27, 28]. Therefore, a fundamental understanding of the particle formation kinetics and reaction pathways is warranted for microstructural control of in situ MMNCs.

A promising in situ approach for creating Al/TiC MMNCs involves reacting a mixture of C powder and a Ti-bearing salt-based flux (dipotassium titanium hexafluoride, K<sub>2</sub>TiF<sub>6</sub>) in an Al melt [2, 19, 25, 26, 27, 28, 29, 30, 31]. When the flux is reduced by the Al melt, it releases solutal Ti following Eq. 1 [25, 26, 32, 33, 34]:

$$3K_2TiF_6(l) + 4Al(l) = 3[Ti] + 3KAlF_4(l) + K_3AlF_6(l)$$
(1)

This method is promising for its improved wetting and infiltration, reduced oxidation, and for its potential to be integrated into a foundry workflow since surface fluxes are already an industry practice. In fact, Lee et al. have found that different compositions of the Ti-bearing flux all produced TiC  $\boxed{31}$ . Once Ti is liberated in the melt via Eq. 1, it can react with either solid C or solutal C to produce TiC; see Eqs. 2-3. Yet this is not the only hypothesized pathway: it is also possible for the solutal Ti to react with Al to form Al<sub>3</sub>Ti, which then reacts with solutal C to form TiC; see Eq. 4. It has also been speculated that TiC can form using Al<sub>4</sub>C<sub>3</sub> as an intermediate phase, but that intermetallic has not been observed in salt flux reactions  $\boxed{20}$   $\boxed{35}$   $\boxed{36}$ .

$$[Ti] + C(s) \to TiC(s)$$
 (2)

$$[Ti] + [C] \to TiC(s)$$
 (3)

$$[\mathrm{Ti}] + 3\mathrm{Al}(l) \to \mathrm{Al}_3\mathrm{Ti}(s), \text{ then } \mathrm{Al}_3\mathrm{Ti}(s) + [\mathrm{C}] \to \mathrm{Ti}\mathrm{C}(s)$$
 (4)

It remains to be determined which mechanism(s) of nanoparticle formation dominate in salt flux reaction synthesis, including what role the  $Al_3Ti$  plays in the production of TiC (if any; see **Eq. 4** above). This question is challenging to answer due to the sub-micrometer length-scale of the TiC particles, which limits

the characterization techniques that can be used to study the reaction. A second, confounding issue is how the TiC nanoparticles interact with secondary phases (e.g.,  $Al_3Ti$ ), post reaction. For example, the nanoparticles may impact the nucleation and growth processes of the secondary phases, thereby influencing their morphologies and distributions in the as-solidified microstructure.

In the past decade, synchrotron-based X-ray microscopy has opened the doors to a number of investigations on MMNCs, including the effects of reinforcing particles on grain growth [37, 38, 39], additive manufacturing [40, 41], ultrasonic processing [42], and void formation [43]. Furthermore, it can be utilized to investigate the intricate morphologies of intermetallic [44, 45, 46, 47] and semiconducting phases [48, 49]. The ability to probe microstructure in 3D gives us an unparalleled opportunity to test the predictions of models and theories. Since such a characterization is nondestructive, it is possible to combine it with other techniques to bring together perspectives from multiple length-scales and imaging modalities [50, 51].

Most of the prior studies listed above harnessed X-ray microtomography, whereas here, we used synchrotron nanotomography based on the transmission X-ray microscope (TXM) to visualize in 3D the complex and multi-phase microstructure of in situ Al/TiC MMNCs and to gain a deeper understanding of salt flux reaction synthesis. Our previous experiments [19] indicated that the TiC particles produced via salt-flux reaction are generally tens of nm in diameter, as alluded to above. In comparison, X-ray microtomography can achieve a pixel size of only  $\sim 1 \mu m^2$ , making it impossible to distinguish individual TiC particles. Instead, with the aid of TXM, we visualize the as-synthesized nanoparticles and their microstructural neighborhoods in a sufficiently large volume (50<sup>3</sup>  $\mu m^3$ ) and at sufficiently high spatial resolution (50<sup>3</sup>  $nm^3$ ). The experiments can be done in under one minute [52], thereby facilitating rapid acquisition of 3D data.

Understanding the details of phase formation during nucleation via real-time experiments poses several challenges. First, achieving rapid cooling rates necessary for undercooled solidification at synchrotron facilities using in situ furnaces is nontrivial, limiting the range of attainable rates. Variable cooling rates can result in diverse morphologies of Al<sub>3</sub>Ti, as will be shown later. Furthermore, rapid cooling necessitates a higher time-resolution, which would compromise the spatial resolution owing to a reduced signal-to-noise 53. Second, due to the complexity of the 3D growth forms, we require 4D experiments; unfortunately, however, the time required for collecting 3D datasets at high spatial resolution (on the order of one minute 52, as noted above) inhibits capturing in real-time nucleation and growth at modest undercoolings. Third, TXM demands small samples, altering solidification conditions and impacting phase formation due to the imposed boundary conditions. Fourth, experimental procedures for in situ studies would involve prohibitively high temperatures (to melt the particles and the intermetallics). Finally, the density of Al<sub>3</sub>Ti is higher than that of Al, and hence the Al<sub>3</sub>Ti crystals will sediment to the bottom of the crucible via gravitational settling; maintaining their position in a stationary state is not feasible. These challenges motivated us to conduct phase-field simulations to provide mechanistic insight on the nucleation and growth of the intermetallic crystals. These simulations enable us to fill in spatiotemporal gaps in the experiments and propose a mechanism for microstructure evolution. Our nanoscopic characterization, together with electron microscopy and the corresponding phase field simulations, allows us to draw important conclusions regarding the *in situ* salt flux reaction pathway as well as the interaction between nanoparticles and secondary phases.

### 2. Experimental details

#### 2.1. Salt-flux reaction synthesis

The *in situ* MMNC samples were prepared using Al shot (99.99%, 2-5 mesh, Belmont Metals) as the metal matrix. K<sub>2</sub>TiF<sub>6</sub> flux (>100 µm, Millipore Sigma) and super activated C (<100 nm, SkySpring Nanomaterials, Inc.) powders were chosen as reactants. They were weighed in a 1:1 molar ratio to target stoichiometric TiC production. The powders were mixed with mortar and pestle until homogeneous, then some was added to the Al for a targeted yield of 3 vol.% TiC. Molten Al at 850 °C has a solubility of 1 wt.% Ti, which would constitute 20 wt.% of the Ti from the flux. While some loss of Ti to the melt is expected, the salt-flux reaction is thought to take place at the liquid flux-melt interface, so it was assumed that a majority of the Ti would react to form TiC rather than dissolve into the melt [26].

In the experiment, approx. 500 g of Al was melted in a 49 mm ID graphite crucible (3 kg capacity) without a protective gas cover in a Lindberg/MPH crucible furnace. Once the melt had reached 850 °C, as measured by an immersion temperature probe (K-type thermocouple), the powder mixture was added on top of the melt and allowed to remain stagnant until the flux liquified fully. The melt was mixed with a BN-coated steel impeller (four 2.5 in. dia. blades) placed at the liquid Al/liquid flux interface rotating at 300 RPM for 10 min. Surface entrainment of air, surface oxide, or flux into the Al matrix during stirring is unavoidable as is known in any industrial setting and can only be minimized. That said, the flux is of sufficiently low density to float to the top of the melt for skimming post-reaction. Subsequently, the melt was poured in a straight line (8-11 mm thick and 25-40 mm wide) onto a chilled Cu plate (1 °C) to prevent particles from settling and thus to ensure their presence in the TXM samples  $\boxed{20}$ .

A surrogate experiment was performed to measure the cooling rate during solidification. For this study, a 99.99% purity Al was heated to 850 °C and poured onto a chilled Cu plate while multiple thermocouples were placed along the path of the pour. Data from the thermocouples was recorded using a DataDI 1100 (DataQ Instruments, Akron, OH). A maximum cooling rate of 24 °C/s was measured immediately after the Al was poured onto the Cu, while a minimum cooling rate was recorded as 2 °C/s.

# 2.2. Multi-modal characterization

As a first step, metallographic specimens for scanning electron microscopy (SEM) were sectioned from the as cast material and then prepared using standard polishing procedures with a 1 µm diamond suspension finishing step. Microstructural characterization (in 2D) was performed using a Tescan MIRA3 field emission gun (FEG) SEM operating in backscatter electron (BSE) mode at 15 kV and a beam intensity of 8-12. An integrated EDAX energy dispersive spectroscopy (EDS) system was utilized for chemical identification. X-ray diffraction (XRD) analysis was performed using a Rigaku SmartLab XRD operating at 40 kV and 44 mA with Bragg-Brentano para-focusing optics and a D/tex Ultra 250 detector.

To obtain a holistic view of microstructure in 3D, we utilized synchrotron-based TXM. For this purpose, 1 mm rods were cut out of the quenched MMNC samples via wire EDM (Cut Rite EDM, Inc.), after which the rods were thinned to a diameter of 80-100  $\mu m$  by electropolishing, as described in our previous work [20]. Subsequently, micropillar specimens approximately 50  $\mu$ m in diameter and 100  $\mu$ m in height were fabricated for TXM from the electropolished rods via Xe<sup>+</sup> plasma focused ion beam (P-FIB) milling with a FEI Helios<sup>TM</sup> G4 P FIB operating at 30 kV and 2.5  $\mu$ A for general milling. Polishing cuts were made using 30 kV and 60 nA. A representative micropillar is shown in **Fig. S1** in the Supplementary Information (SI).

Following sample preparation, we conducted nanotomography measurements with the TXM at the Full-field X-ray Imaging beamline 18-ID at Brookhaven National Laboratory's National Synchrotron Light Source II (Upton, NY, USA). A monochromatic X-ray beam operating at 7 keV illuminated the sample, then a zone plate used as an objective lens with 323× magnification focused the forward transmitted beam onto an Andor Neo 5.5 detector that is coupled with a 10× optical objective lens. The pixel size on the detector measured  $20^2$  nm<sup>2</sup>, with a FOV of  $51.2 \times 43.2 \ \mu m^2$ . A more detailed description of the experimental setup can be found elsewhere [54]. During data acquisition, the sample was rotated at 2 °/s from 0 to 180°, with an exposure of 0.1 s, thus giving 900 projection images. We used these projections to reconstruct the sample volume in 3D using TomoPy, a Python-based open source framework for tomographic data processing [55]. We first subtracted a dark background image from each projection image, normalized them with a reference illumination beam image, then removed "ring" artifacts [56], and finally reconstructed the data used the Gridrec algorithm, a direct Fourier-based method with a Parzen window filter [57]. Further data processing was done in the MATLAB R2020b computing environment (Natick, MA, USA).

Sufficient absorption contrast at 7 keV enabled identification of the phases present in the microstructure, namely, the Al matrix (dark gray), Al<sub>3</sub>Ti intermetallic (intermediate gray), and TiC (light gray); see Fig. S2 in the SI. A histogram of the grayscale intensities of the phases within the reconstructed TXM data is shown in Fig. S3 in the SI, and theoretical attenuation lengths, attenuation coefficients, crystal structures, and other pertinent information for these and other potential phases that may form during the salt-flux reaction are shown in Table S1 in the SI. Values for density  $\rho$  and attenuation length  $L_{atten}$  are taken from Refs. [58] and [59], respectively. Accordingly, the linear and mass attenuation coefficients  $\mu_L$  and  $\mu_M$  can be calculated as  $\mu_L = 1/L_{atten}$  and  $\mu_M = 1/(L_{atten}\rho)$ , respectively. In the SI, we also quantify the resolution of TXM technique using a Fourier-based criterion [60] [61] and demonstrate an effective spatial resolution of  $\sim$ 50 nm (see Fig. S4). The high fidelity of the TXM reconstruction thus enables a quantitative 3D analysis.

To gain a comprehensive understanding of the localized features observed in the TXM data, we used high-resolution scanning transmission electron microscopy (HR-STEM). For this purpose, TEM lamella samples were prepared from the bulk specimen utilizing the Focused Ion Beam (FIB) lift-out technique, employing a FEI Helios<sup>™</sup> scanning electron microscope (SEM) with parameters analogous to those used in preparing micropillars for TXM. Subsequent scanning/transmission electron microscopy (S/TEM) imaging was performed using the Thermo Fisher Scientific Talos F200X G2 S/TEM, operating at an accelerated

voltage of 200 kV.

Additionally, the same sample prepared for S/TEM was investigated via Transmission Kikuchi Diffraction (TKD) to determine the crystallographic orientation of one of the Al<sub>3</sub>Ti morphologies (the so-called "orthogonal plates", described below). Another region of this sample, featuring nearly perpendicular plates of Al<sub>3</sub>Ti, was specifically chosen for Electron Backscatter Diffraction (EBSD) to ensure a comprehensive, cross-sectional perspective. These samples were ion-milled using the Focused Ion Beam (FIB) technology within the FEI Helios<sup>TM</sup> SEM, allowing seamless acquisition of TKD and EBSD patterns within the same instrument setup. To ensure high-quality Kikuchi patterns, the samples were cleaned at a voltage of 5 keV to eliminate any surface damage before data acquisition.

#### 3. Results

#### 3.1. Taxonomy of intermetallic morphologies

The SEM image in **Fig. 1(a)** shows Al<sub>3</sub>Ti intermetallics of various sizes and shapes (green arrows). Generally, we observe overlapping plates of various orientations, although there is also one large individual plate (orange arrow at top-left). TiC particles (red arrows) can be seen as agglomerates in the grain boundaries, likely pushed there during solidification **62**. KAlF<sub>4</sub> particles (black arrows), produced from the reaction between the flux and Al, can be seen within the TiC agglomerates as small black circles. For typical use of K<sub>2</sub>TiF<sub>6</sub> flux, the KAlF<sub>4</sub> and other byproducts are removed from the melt *via* degassing and can be found in the dross **2**, **26**, **28**, **63**, but we did not perform this step prior to quenching. XRD peaks for TiC, Al<sub>3</sub>Ti, and KAlF<sub>4</sub> can be seen in **Fig. 1(b)**, verifying that both TiC particles and Al<sub>3</sub>Ti intermetallics were created during the *in situ* process. There is no sign of excess C in either the SEM or XRD, likely because it stays afloat in the liquid flux layer and is skimmed off before pouring.

A 3D visualization can help us determine if the overlapping plates of Al<sub>3</sub>Ti are single, contiguous structures or agglomerated, independent entities. **Fig. 2(a)** shows a representative TXM reconstruction, wherein the TiC is illuminated in red and the Al<sub>3</sub>Ti in green, and the edges of the sample in translucent blue. From this data, we calculated the volume fraction of the TiC and Al<sub>3</sub>Ti to be 3.3 and 0.8 vol.%, respectively, which is close to the expected 3.0 vol.% TiC (vide supra). **Fig. 2(b)** displays only the Al<sub>3</sub>Ti phase, for clarity. Multiple contiguous structures of Al<sub>3</sub>Ti were discovered therein, including "orthogonal plates" (**Fig. 2(c)**), "individual plates" (**Fig. 2(d)**), cuboids (**Fig. 2(e)**), and large blocks (**Fig. 3**). The renderings on the left in **Figs. 2(c-e)** show the smallest intermetallic of the given morphological type found in the data, while those on the right depict a more developed version of that morphology (presumably at a later stage in the growth process, after a growth instability sets in and accentuates the corners of the three structures [64, 65, 66]). In all, 41 orthogonal plates, 18 individual plates, 11 cuboids, and 3 groups of large blocks were found in the TXM data. That the Al<sub>3</sub>Ti phase is faceted in all cases is expected given that the Jackson α-factor exceeds the threshold value of two (above which layer growth is predicted [67]). Nevertheless, the great diversity of Al<sub>3</sub>Ti nanostructures is surprising and calls for further analysis, especially since their morphology can directly impact mechanical properties [68].

The morphology of Al<sub>3</sub>Ti has been shown to be highly dependent on the cooling rate [27, 28, 68, 69, 70, 71, 72, 73, 74]. To measure the cooling rates during solidification, a surrogate experiment was conducted as detailed in Sec. [2.1]. The obtained cooling rates fall within the range of 2-24 °C/s. According to existing literature, this range of cooling rates typically results in the formation of plate-like Al<sub>3</sub>Ti structures, often termed "flaky" or "needle-like", resembling those depicted in Fig. 2(d). At the lower cooling rates in this range, coarser and blocky formations of Al<sub>3</sub>Ti are expected to emerge, akin to those shown in Fig. S5 in the SI and Refs. [27, 28, 68, 69, 70, 71, 72, 73, 74]. Those studies align with ours, offering an explanation for some of the diverse intermetallic morphologies visualized herein.

The origins of the cuboids and orthogonal plates remain far less clear. It has been suggested by El Mahallaway et al. that Al<sub>3</sub>Ti rich in Ti (closer to Al<sub>2</sub>Ti), tends towards a cuboid shape, or that the cuboid is a more developed version of a globular Al<sub>3</sub>Ti precipitate [29]. On the other hand, Majumdar and Muddle found similar cuboid structures and identified them as Al<sub>3</sub>Ti in a metastable  $\beta'$  phase of composition Al-20wt.% Ti (space group: Pm $\bar{3}$ m, Strukturbericht designation: L1<sub>2</sub>) [74]. An inhomogeneous distribution of Ti in the melt may have led to similar trends as seen in these two studies since some regions of the TXM data showed a local volume fraction of the TiC exceeding the expected overall volume fraction of 3 %. This would imply a chemical segregation of Ti in the melt. Small globular Al<sub>3</sub>Ti (with equivalent radii < 1  $\mu$ m) was also found in the TXM data, but their small size made it difficult to discern if they were precursors to cuboid shapes or would grow into other morphologies. Of note is that other Al-containing intermetallics have cuboidal shapes, such as Al<sub>3</sub>Zr, Al<sub>3</sub>Hf, and Al<sub>3</sub>Sc [73, [75, [76]], and all have also shown a pronounced morphological sensitivity to cooling rate [73, [75, [76]]. Therefore, it is plausible that the Al<sub>3</sub>Ti cuboids are either due to macrosegregation of solutal Ti, leading to Ti-rich (or poor) Al<sub>3</sub>Ti intermetallics, or otherwise from impurities in the matrix.

Previously, researchers have attributed the orthogonal plates of Al<sub>3</sub>Ti to multiple twinning [77] or else did not study them in depth [9, 25]. There are multiple examples of thin flakes of Al<sub>3</sub>Ti forming perpendicular structures, although they tend to be much larger ( $\gtrsim 5 \mu m$ ), more dendritic, and obtained under far lower cooling rates ( $\lesssim 1$  °C/s) [27, 28, 68, 69, 70, 71, 72, 73, 74]. Importantly, in our work, the TXM data reveals particles (later proved to be TiC) at or near the intersection of the orthogonal Al<sub>3</sub>Ti plates; see Fig. 3(a). In comparison, there are no such instances of TiC particles embedded within any of the other Al<sub>3</sub>Ti structures nor any other consistent relationships between the two phases. That said, there are a few examples of TiC on/near the surface of the intermetallics, likely pushed by Al<sub>3</sub>Ti during its growth.

Based on these observations, we propose that the orthogonal plate morphology arises during nucleation, i.e., the Al<sub>3</sub>Ti phase nucleates heterogeneously on the TiC particle (crystal structure: cubic, Fm $\bar{3}$ m) and grows epitaxially on its solid-liquid interfaces. Importantly, due to non-reciprocal nucleation theory [78, 79], if TiC is nucleating Al<sub>3</sub>Ti, then the converse cannot be true, thus ruling out the indirect route of TiC formation via the breakdown of Al<sub>3</sub>Ti by Eq. 4 (in general, non-reciprocal nucleation postulates that there exists a significant disparity in the undercoolings required for the heterogeneous nucleation of phase  $\alpha$  on

substrate  $\beta$  compared to phase  $\beta$  on substrate  $\alpha$ ). It also follows that the TiC forms by salt-flux reaction prior to the Al<sub>3</sub>Ti intermetallic. It has been shown that Al<sub>3</sub>Ti can nucleate heterogeneously on TiB<sub>2</sub> [29, 81] and on Al<sub>2</sub>O<sub>3</sub> [82] but neither of these processes results in an orthogonal plate structure. Below, we offer evidence to support our hypothesis on the emergence of this unexpected morphology.

#### 3.2. Origin of orthogonal plate structures

First, we investigate the directionality of the  $Al_3Ti$  structures that contain particles within. The normal vectors along the  $Al_3Ti$ -Al interfaces can be projected stereographically to yield a so-called interfacial normal distribution (IND); see Ref. [83]. The zone axis for the calculation is represented by the pink arrow in Fig. 3(a), and the corresponding IND is shown in Fig. 3(b). The peaks along the edge of the primitive circle represent a preponderance of normal vectors with a given orientation in the specimen frame — in this case, they come from the broad faces that are  $\sim 90^{\circ}$  away from the zone axis (in pink), and also  $\sim 90^{\circ}$  away from one another. This confirms that the plates are indeed orthogonal to one another, and this is no coincidence. There is some noise in the IND due to the fact that TiC particles sometimes border the surfaces of  $Al_3Ti$ ; these particles were removed for the IND analysis in order to focus exclusively on the directionality of the intermetallics. The orthogonality of the  $Al_3Ti$  plates is consistent with an underlying cubic symmetry, which is naturally absent in the  $Al_3Ti$  crystal structure (body-centered tetragonal, refer to Sec. [4.2]). Therefore, we hypothesize that this orthogonality originates from the symmetry of the nucleant particle.

While the basic structure of three intersecting orthogonal plates was common, many intermetallic structures had "extra" plates growing in parallel to basic ones (see **Figs. 3(c,e)**), or had extraneous plates unrelated to these ones. The additional planes are likely caused by crystallographic twinning of Al<sub>3</sub>Ti 85, 66, and/or by stress that develops in the evolving structure during solidification.

Some other orthogonal plates had one or multiple plates underdeveloped. **Fig. 3(c)** shows two such Al<sub>3</sub>Ti orthogonal plate structures that grew next to each other (but were misaligned from one another). The plates located between the two structures are stunted in comparison to the rest of the plates. This underdevelopment is reasonable given that the two intermetallics share the same Ti solute field (a "soft" collision in solidification [64], leading to competitive growth). We plotted the INDs of both structures; see **Fig. 3(d)**. The zone axis is given as the pink vector associated with the structure at right. In this case, the IND represents the superposition of two independent crystals: those hotspots with the white arrows come from the left-hand, or "misaligned" intermetallic (in this frame-of-reference). The misorientation between the two structures is about 15-30° off-axis, depending on the axis.

Fig. 3(e) shows a single  $Al_3$ Ti structure with two large TiC embedded within, and two parallel plates in each orthogonal direction. The distance between the centroids of the two TiC particles was found to be 202 nm, while that between the two parallel plates was  $197\pm21$  nm (obtained from 12 measurements). The

<sup>&</sup>lt;sup>1</sup>The external morphology of the nucleant reflects its point group isogonal with its space group 84.

agreement between the particle and plate distances suggests that this structure was formed by two individual Al<sub>3</sub>Ti orthogonal plate structures nucleating on separate TiC particles; during growth, the two impinged on one another (a "hard" collision in solidification) and likely rotated over time to reduce the grain boundary energy [87], [88]. This rotation could be accomplished *via* rigid sliding of one intermetallic with respect to the other along their shared boundary [88]. The IND of this coalesced structure is shown in **Fig. 3(f)**. It depicts an almost-perfect alignment of the plates in each direction, *cf.* **Fig. 3(b)**.

The TXM experiment provides not only morphological information but also detailed chemical information. This is because the grey-scale value of each voxel in the reconstruction is linearly related to the attenuation coefficient of the sample at the position of the voxel. With this in mind, we used the greyscale intensity values to identify the phases more conclusively, with attention to the bright particle(s) within the orthogonal Al<sub>3</sub>Ti plates. Using the methodology outlined by Ebner *et al.*  $\mathbb{SQ}$ , we normalize the intensity values of the Al/TiC MMNC sample, using two internal standards for the normalization (see **Table S2**). One is the air that is outside the sample, and the other is the Al matrix. The Ti solubility in Al at room temperature is low enough that it is reasonable to assume the matrix is essentially pure Al. From these two values, we determine the linear normalization function,  $\mu_L = aW + b$ , where W is the grayscale intensity value and a and b are constants (7.96E-5 1/cm and -70.27 1/cm, respectively). Accordingly, we predict the greyscale intensity values W for all phases which could have formed during the salt-flux reaction synthesis, using their theoretical linear attenuation coefficients  $\mu_L$  as input (see **Table S1** for possible phases and **Table S3** for calculated intensity values). Conversely, we predict the linear attenuation coefficients  $\mu_L$  for the phases in the TXM data using their intensity values W (see **Table S2**). This enabled a direct assessment of the chemistry of the phases in the TXM data, which we later confirm via TEM (vide infra).

In **Table S4**, we compare between theoretical and calculated values for  $\mu_L$  and W. The top portion considers the Al, air, and Al<sub>3</sub>Ti, while the lower portion compares the values for the core particles with all possible cubic, tetragonal, trigonal, and orthorhombic phases, as all those structures have internal angles of 90° (between like or unlike planes) and could explain the symmetry of the orthogonal plate structures. As expected, the percent error for air and Al is nil as they were used for the normalization function, but for the intermetallics (plate and orthogonal plate structure), there is consistently a  $\sim 10\%$  error. This may suggest some systematic error in the normalization procedure (more than two standards would increase the accuracy of this method). Alternatively, the intermetallic may well be off-stoichiometry, such that there is 5-10% more Ti than would be anticipated 90.

The results in the bottom portion of **Table S4** rule out several possible phases for the core particle as their intensities and linear attenuation coefficient values do not fall within the systematic error range noted above. The only phases with  $\mu_L$  and W that are remotely close to the experimental values include a high temperature Ti cubic phase and TiC; however, the former is not likely since its transition to cubic Ti occurs at 882 °C (assuming thermodynamic equilibrium), which is well above our operating temperature. Furthermore, we did not find evidence for pure Ti in SEM, XRD, or TEM. It follows that the core particle

is most likely TiC, although the match is not perfect. If not for a systematic error, the core TiC particles may be off-stoichiometry, much like the intermetallics. It has been shown previously that TiC often forms in sub-stoichiometric Ti/C ratios in salt-flux reaction, ascribed to C vacancies in the TiC lattice [91]. In this case, we can expect that there are far more C-vacancies in the core TiC particle than in TiC<sub>0.95</sub>, which should result in an increase in its greyscale value W.

Fig. 4 shows the distribution of the TiC particle sizes (measured as equivalent radii R). The size range in the histogram is limited to those TiC particles that are discernable, *i.e.*, particles of size R < 50 nm were ignored as they are approaching the spatial resolution of TXM, and likewise particles of size R > 500 nm were assumed to be large agglomerates and therefore not considered here. The brown bins of the histogram represent the subset of TiC particles that were found to be at or near their center of the Al<sub>3</sub>Ti orthogonal plates, *i.e.*, the heterogeneous nucleating sites (see also the inset of Fig. 4). It was found that the average size over all particles is  $160\pm99$  nm, while that for the TiC nucleants is  $290\pm59$  nm.

The above analysis suggests that there is a minimum size of TiC required for heterogenous nucleation of Al<sub>3</sub>Ti. To rationalize this result, we invoke the free-growth model by Greer and coworkers [92], [93], [94]: particles (here, TiC), with faces of size R' are ideally wet by a crystal (here, Al<sub>3</sub>Ti); they remain dormant until the radius of the homogeneous crystal nucleus becomes smaller than R' and free growth sets in. This will occur at a particular undercooling  $\Delta T_{fg} = \frac{2\gamma}{\Delta S_V R'}$  where  $\gamma$  is the interfacial free energy between the crystal and liquid, and  $\Delta S_V$  is the entropy of fusion per unit volume of the crystal. In a polydisperse system (i.e., one with a range of particle sizes, such as ours), it follows that all particles of size R' and greater will be activated at an undercooling of  $\Delta T_{fg}$ . Using  $\Delta S_V \cong 1.3 \frac{J}{cm^3 K}$ ,  $\gamma = 0.074 \frac{mJ}{cm^2}$  [95] and, at minimum,  $R' = 4 \times 10^{-5}$  cm (see Fig. 4), we find  $\Delta T_{fg} \cong 6$  °C. Given the reaction occurs at 850 °C, this would imply a liquidus temperature of 856 °C for Al<sub>3</sub>Ti, which corresponds to an alloy of composition Al-1wt.% Ti (the solubility limit of Ti in Al). Hence, about one quarter of the Ti by weight from the K<sub>2</sub>TiF<sub>6</sub> did not react to yield TiC. This conclusion reasonably fits the volume fractions of TiC and Al<sub>3</sub>Ti that we measured via TXM, reaffirming the amount of Ti which did not form TiC. The self consistency also provides support for the free growth model for heterogeneous nucleation [2].

#### 3.3. Intermetallic morphologies without TiC

To assess the influence of TiC on Al<sub>3</sub>Ti morphology, we conducted an additional experiment under identical processing conditions. However, in this case, we omitted the carbon necessary for TiC formation. That is, this control experiment led to the formation of Al<sub>3</sub>Ti in the absence of TiC, providing a basis for comparison with the samples containing TiC. The results are depicted in **Fig. 5**, showcasing the morphological differences observed with and without TiC. Importantly, we find that the presence of TiC resulted in orthogonal plate morphologies, distinct from those blocky structures observed in the absence of TiC. The latter case would

<sup>&</sup>lt;sup>2</sup>The suitability of the free-growth model in this study would suggest that the anisotropy of the solid-liquid interfacial free energy of the TiC nucleant is relatively weak [96].

suggest a difficulty in achieving cube-symmetric orthogonal plate structures solely through the tetragonal symmetry of  $Al_3Ti$ . It follows that TiC must catalyze the formation of the orthogonal plates. Finally, we note that despite the consistent supply of titanium through the flux in both scenarios, the absence of TiC resulted in a relatively higher volume fraction of  $Al_3Ti$ , owing to the fact that more Ti remains in the liquid (*i.e.*, it is not tied up in the salt flux reactions; see Eqs. 2-4).

#### 3.4. Epitaxy between particle and intermetallic

We employed scanning transmission electron microscopy (STEM) to investigate the interface between the two solid phases, aiming to gain deeper insights into the efficacy of  $Al_3Ti$  nucleation on TiC. **Fig. 6(a)** shows a low-magnification bright-field STEM image of an  $Al_3Ti$  plate. We magnified a region of interest denoted by the white dotted circle in **Fig. 6(a)**; see the high resolution STEM micrograph in **Fig. 6(b)**. This image unequivocally establishes the presence of coherency between  $Al_3Ti$  and TiC phases.

To further elucidate the crystallographic relationship between the phases, we conducted simulations of electron diffraction along the [010] beam direction via fast Fourier transform. Figs. 6(c-d) give the diffraction patterns corresponding to Al<sub>3</sub>Ti and TiC, respectively. The observed diffraction patterns convey an orientation relationship (OR) between the (002) planes of Al<sub>3</sub>Ti and TiC phases. For this same OR, it is possible to coincide the {110} family of planes for both crystals, as shown stereographically in Fig. S6 in the SI.

While this specific TiC particle does not serve as the central "core" particle, situated at the centre of the orthogonal plates and initiating the nucleation of the intermetallic, it serves as a suitable surrogate to validate the potential epitaxial relationship between Al<sub>3</sub>Ti and TiC. Note there is only a 5% chance that a randomly-oriented plane will intersect the larger TiC particles that are capable of nucleating Al<sub>3</sub>Ti at the aforementioned undercooling  $\Delta T_{fg}$ . A second confounding issue is that the milling depth achieved by a single FIB pass is on the same order of magnitude as the particle diameter, preventing its successful capture. Instead, the smaller particle shown in **Fig. 6** likely encountered the surface of an already-nucleated Al<sub>3</sub>Ti intermetallic and underwent rotational repositioning to minimize the interphase boundary energy, a common occurrence in semi-solid sintering 87.

In Fig. 7, we examine these smaller particles more closely. Fig. 7(a) shows a STEM image wherein Al<sub>3</sub>Ti is dark gray, TiC is black and dotted, and the Al matrix is light gray. The Al<sub>3</sub>Ti intermetallic shows a splitting of its plates (see green arrows) with TiC particles wedged between them. Fig. 7(b) is a HAADF image of the boxed region in Fig. 7(a) depicting clusters of TiC (marked with red arrows) trapped between intermetallic plates. Figs. 7(c-e) are HAADF images which verify that these particles have high concentration of Ti and C, as expected. Some examples of entrapped Al were also found in the TXM data, although, for simplicity, this phase was left out of the 3D visualizations (Figs. 2-3).

<sup>&</sup>lt;sup>3</sup>According to Fig. 4, the so-called larger particles are  $0.25 \mu m$  in size. About 10 of them are in a TXM scan (see Fig. 2(b)), where the sample dia. is  $50 \mu m$ . Thus,  $0.25 \times 10/50 = 0.05$ , or a probability of 5%, assuming uniformly distributed particles

The STEM images reveal that the TiC particles have dual effects on the morphology of Al<sub>3</sub>Ti: those TiC particles above a critical radius of curvature act as nucleants for the Al<sub>3</sub>Ti, leading to the formation of the orthogonal plate structures; meanwhile, the smaller TiC particles perturb the growth process of the intermetallic, similar to how grain-refining particles split dendrite arms during free growth [21] [37] [38] [39]. The presence of the small carbides in the liquid may either disrupt the local solute field [97] [98], leading to variations of the driving force for solidification, or else collide with the Al<sub>3</sub>Ti growth front directly. The exact mechanism remains a topic for future study. Due to the strong crystalline anisotropy of Al<sub>3</sub>Ti [68], the two branches of Al<sub>3</sub>Ti maintain their facets, grow in parallel, and never coalesce. This phenomenon can be seen in 2D with SEM (Fig. 1(a)) and in 3D with TXM (Fig. 3(c)). A corollary of this finding is that the TiC particles were not uniformly dispersed in the melt: single plates of Al<sub>3</sub>Ti found in the TXM data (refer again to Fig. 2(d)) did not show this splitting behavior, which would imply that these plates nucleated in regions devoid of the TiC particles.

#### 3.5. Crystallographic orientations of orthogonal plates

To discern the crystallographic orientations of the orthogonal plate structures, TKD was performed on the same sample examined above in TEM. The results are presented in **Fig. 8**, wherein the inverse pole figures convey the orientations of the distinct grains of  $Al_3Ti$ . These pole figures reveal that the broadest surfaces of the plates are bounded by  $\{001\}$  planes, while the narrow surfaces are oriented  $\{100\}$ , as schematized in **Fig. 8(d)**. Given the orthogonality of the structure, the two plates imaged are misoriented by  $90^{\circ}$ .

To corroborate these findings, EBSD was conducted on a different orthogonal plate structure; see Fig. 9, where again the plates exhibit an approximate perpendicular alignment. The resultant pole figures (Figs. 9(a-b)) correspond to the orthogonal plates boxed in blue and red, respectively, consistently illustrating that the largest surfaces of Al<sub>3</sub>Ti are constituted by {001} planes, while the complementary set of interfaces are formed by {100} planes. These findings are distilled in the schematic given in Fig. 9(e). Taken altogether, this picture suggests that that the orthogonal plates are not the product of a growth-front instability of a *single* grain, but instead the simultaneous formation of *multiple* grains. That said, individual plates of the orthogonal structure may later split into two branches due to disruptions in the local solute field, as noted above in Sec. [3.4].

#### 3.6. Phase-field simulations

To lend credence to the above ideas, a phase-field model was constructed to examine the formation of orthogonal Al<sub>3</sub>Ti plates on TiC particles. Each Al<sub>3</sub>Ti plate was described by a solidification model developed by Folch *et al.* [99] with an anisotropic interfacial energy to match the experimentally observed Al<sub>3</sub>Ti shape. To simulate multiple Al<sub>3</sub>Ti plates on the same nucleant particle, we adopted the multi-order-parameter approach developed by Fan *et al.* [100]. We closely followed the implementation by Ofori-Opoku *et al.* [101], in which this approach was applied to a solidification model. Additionally, we incorporated the Extended Smooth Boundary Method [102] to introduce an inert TiC particle serving as the nucleant substrate. The

governing equations were solved using the PRISMS-PF framework [103], [104], an open-source phase-field equation solver. Additional details regarding the model and parameters can be found in the SI. The use of these well-established phase-field models for our simulations, as well as the parameterization that is calibrated to qualitatively match the experimental observations, ensures an accurate representation of essential physical processes occurring in the experimental system, including heterogeneous nucleation and solidification with anisotropic interfacial energy.

In an effort to unravel the formation mechanism for the orthogonal morphology of  $Al_3Ti$ , we considered various initial placements of the nuclei on planes of cubic symmetry. Specifically, we simulated using a different number of grains on different TiC planes, as shown in **Table S6**. We focused particularly on TiC  $\{100\}$  and  $\{110\}$  planes, given that nucleation on  $\{111\}$  planes cannot lead to orthogonal symmetry. For the  $\{100\}$  planes, we tested nucleation on three and six sites. While the arrangements of three and six grains allowed for orthogonal growth, they did not lead to the targeted morphology. For  $\{110\}$  planes, fewer than 12 grains resulted in missing plates in the orthogonal structure. Ultimately, the simulations indicate that 12 nucleated grains of  $Al_3Ti$  are required to form the orthogonal structures seen experimentally.

# 4. Discussion

# 4.1. Formation of TiC nanoparticles

According to our interpretation, the formation of TiC precedes that of Al<sub>3</sub>Ti. Consequently, the coexistence of TiC with liquid Al saturated in solutal Ti triggers the nucleation and growth of Al<sub>3</sub>Ti (discussed in detail below). This line of reasoning finds support in both the existing literature on the ternary Al-Ti-C phase diagrams [105, 106, 107] as well as our experimental observations: notably, we observe TiC embedded within the Al<sub>3</sub>Ti structures. Alternatively, if Al<sub>3</sub>Ti were to form as an intermediate, later reacting with C to produce TiC according to Eq. 4, we would expect to see TiC at the interface between Al<sub>3</sub>Ti and the C-enriched liquid. Such an occurrence is not evident in the TXM data. In addition, we do not see small particles (< 50 nm dia.) within the intermetallic crystals via higher resolution imaging in TEM (note such small particles are below the spatial resolution of TXM).

#### 4.2. Formation of Al<sub>3</sub> Ti single and orthogonal plates

Al<sub>3</sub>Ti is a body-centered tetragonal (BCT) crystal, characterized by Laue symmetry 4/mmm, with lattice parameters a = 0.386 and c = 0.868 nm (space group: I4/mmm, Strukturbericht designation: DO<sub>22</sub>). The growth morphology of Al<sub>3</sub>Ti depends on its crystallographic anisotropy and cooling rate, as noted previously. For instance, the slower growth of  $\{001\}$  planes is anticipated due to factors such as bonding and packing fraction [108]. Consequently, these slow-growing planes can manifest as the larger surfaces of the single Al<sub>3</sub>Ti plates, as evidenced by **Figs. 8-9**. The EBSD results in particular suggest that a growth tip along <110> is formed with (100) and (010) facet planes, as depicted in **Fig. 9**. Moreover, growth along <110> is expedited owing to looser atomic packing in that direction and/or micro-facets of  $\{100\}$ . With minimal growth in the direction normal to the (001) plane, the process is confined to two-dimensions. The growth

orientation and morphology of individual plates shares semblance to other faceted crystals growing in a diffusion field [44, 45, 49, 46, 47].

The formation of the orthogonal plates shares similar growth characteristics to the single plate, but the key distinction lies in the fact that there are three set of plates growing perpendicular to each other, originating from a common site. Relying on kinetic arguments alone is not sufficient to explain the spontaneous emergence of three mutually perpendicular grains (nor is the orthogonal plate structure seen in the control Al-Ti sample). Therefore, we investigated the potential role of TiC in shaping the Al<sub>3</sub>Ti structure. TEM analysis (Fig. 6) reveals the alignment between the (001) of TiC and (001) of Al<sub>3</sub>Ti, as well as that between [100] of TiC and [100] of Al<sub>3</sub>Ti. This alignment is based on the orientation of the TEM lamella with respect to the crystallographic coordinates. Based on the same OR between both phases, it follows that (110) of TiC must align with (110) of  $Al_3$ Ti (the growth tip of the plates, from above). The interface between (110) TiC and (110) Al<sub>3</sub>Ti is hence key for the formation of the orthogonal plate structures, refer again to the stereographic diagram shown in Fig. S6 in the SI. TiC has 12 symmetrically equivalent planes within the  $\{110\}$  family, including (110),  $(\bar{1}\bar{1}0)$ ,  $(\bar{1}\bar{1}0)$ ,  $(\bar{1}10)$ ,  $(\bar{1}01)$ , (101), (101), (101), (011), (011), (011), (011), (011), and each of them is parallel to the growth tip of Al<sub>3</sub>Ti. Hence, this bicrystallography is consistent with the growth morphology of three intersecting plates (and a total of 12 growth tips) of Al<sub>3</sub>Ti. In contrast, other interfaces of TiC like {100} or {111} only have four and eight symmetrically equivalent planes and cannot support the formation of orthogonal plate structures, as confirmed via phase field simulations.

To understand why nucleation may preferentially occur on the  $\{110\}$  planes, we investigate the disregistries between Al<sub>3</sub>Ti and TiC for various combinations of surface planes, assuming coherent interfaces. Bramfitt [109] gives a method to quantify the planar disregistry level between a potential pair of a nucleus surface (denoted by a subscript n) and a substrate surface (denoted by a subscript s). The Bramfitt disregistry is found as [109]

$$\delta_{(hkl)_n}^{(hkl)_s} = \sum_{i=1}^3 \frac{|d_{[uvw]_s}^i \cos \theta - d_{[uvw]_n}^i|}{3d_{[uvw]_n}^i} \times 100$$
 (5)

Here, (hkl) represents a low-index plane, [uvw] is a low-index direction in (hkl),  $d_{[uvw]}$  is the interatomic spacing along [uvw], and  $\theta$  is the angle between  $[uvw]_n$  and  $[uvw]_s$ . The expression takes into account the three lowest-index directions (indicated by subscript i) within the first quadrant of the interface plane. According to Bramfitt [109], a surface is active as heterogeneous nucleation site when  $\delta^{(hkl)_s}_{(hkl)_n}$  is less than 12%. Notably, if  $\delta^{(hkl)_s}_{(hkl)_n}$  is under 5%, the interface is expected to remain coherent [110]. In **Table 1**, the Bramfitt planar disregistries between Al<sub>3</sub>Ti and TiC for potential low-index ORs are presented. As the table indicates, there is significant potential for nucleation on TiC  $\{110\}$  planes. See **Fig. 11** for a schematic illustration. The disregistry level between Al<sub>3</sub>Ti  $\{110\}$  and TiC  $\{110\}$  is lower than the coherence threshold from above.

The calculated misfit between (110) planes of  $Al_3Ti$  and TiC is also lower (4.77%) than that of other sets of planes such as (100) or (111) (**Table**  $\boxed{1}$ ). This point lends support to the idea that (110) planes

| Potential ORs                 | $\delta_{(hkl)_n}^{(hkl)_s}/\%$ |
|-------------------------------|---------------------------------|
| $(110)_{Al_3Ti}, (110)_{TiC}$ | 4.77                            |
| $(112)_{Al_3Ti}, (111)_{TiC}$ | 7.96                            |
| $(100)_{Al_3Ti}, (100)_{TiC}$ | 21.8                            |
| $(400)_{Al_3Ti}, (100)_{TiC}$ | 21.85                           |

Table 1: Bramfitt planar disregistry  $\delta_{(hkl)_n}^{(hkl)_s}$  between Al<sub>3</sub>Ti and TiC for some close-packed planes.

of TiC nucleate (110) planes of Al<sub>3</sub>Ti. As noted previously, Al<sub>3</sub>Ti is tetragonal while TiC is cubic, thus necessitating three sets of Al<sub>3</sub>Ti grains to complete the orthogonal plate structure aligned with {110} of TiC (cf. TKD/EBSD data in Figs. 8-9). It follows that a single nucleant with the requisite cubic symmetry, such as a TiC particle, is more likely than multiple clustered TiC particles. That is, a single TiC particle nucleates a total of 12 grains of Al<sub>3</sub>Ti, four of which exhibit the same orientation (see Sec. [3.6]), i.e., there are three misoriented grains of Al<sub>3</sub>Ti. The growth mechanism is summarized in Fig. 12(a-c). Fig. 12(d) presents a high-magnification image from a deeply etched specimen, revealing the orthogonal structure and noticeable gaps between individual plates. Finally, if the three grains form at different times, the orthogonal plate structures will not be perfectly symmetric — some plates will be longer than others, as shown in Fig. 3.

#### 5. Conclusions

We have undertaken a multi-scale, multi-modal experimental and computational investigation to study Al/TiC MMNCs produced *via* salt-flux reaction, with a focus on the formation of TiC nanoparticles and their impact on the final microstructure. Several conclusions can be drawn from this study:

- 1. There exists not a singular but a diversity of Al<sub>3</sub>Ti growth forms that are obtained in this *in situ* process, including single plates, orthogonal plates, and cuboidal structures. They are caused by different cooling rates, Ti concentrations, and nucleation modes.
- 2. Those intermetallics with the orthogonal plate structure are a direct result of Al<sub>3</sub>Ti nucleating on TiC. Consistent with the prediction of free-growth theory, we find a critical radius of TiC above which heterogeneous nucleation can occur at a given undercooling.
- 3. The crystallographic orientations of the orthogonal plates, together with phase field simulations, indicate that 12 grains of Al<sub>3</sub>Ti nucleate on the {110} interfaces of TiC. If the grains form at different times and/or grow at different rates (depending on the local supersaturation), the orthogonal plates are not symmetric with respect to the core TiC particle.
- 4. TiC particles smaller than the critical size threshold for heterogeneous nucleation (200 nm dia.) may contribute to a branching of the already nucleated Al<sub>3</sub>Ti plates during free growth. This demonstrates a secondary, and often overlooked, effect of the carbide on the intermetallic morphology.
- 5. Due to non-reciprocity of heterogeneous nucleation, TiC cannot nucleate on  $Al_3Ti$ . Furthermore, the 3D reconstructions from TXM suggest that TiC forms before  $Al_3Ti$ . Accordingly, we can rule out

indirect formation mechanisms of TiC which require  $Al_3$ Ti as an intermediary step. It follows that the TiC forms directly from the salt-flux reaction.

Based on the above findings, we hypothesize that orthogonal  $Al_3Ti$  structures would arise in heterogeneous nucleation when the following three conditions are met: (1) the nucleating agent is thermodynamically stable, (2) it has cubic symmetry, and (3) it exhibits epitaxy with  $Al_3Ti$ . More broadly, the detailed characterization presented herein can lead to an informed production of MMNCs via salt flux reaction. Understanding the formation pathway of TiC nanoparticles and their interaction with secondary phases in solidification brings us one step closer to optimizing the heterogeneous microstructure of MMNCs.

#### 6. Acknowledgment

The authors acknowledge the University of Michigan College of Engineering for financial support and the Michigan Center for Materials Characterization for use of the instruments and staff assistance. We also thank David Weiss at Eck Industries and Steven Udvardy at the North American Die Casting Association for helpful discussions, as well as Colin Romine for assistance in sample fabrication. This research used resources of 18-ID of the National Synchrotron Light Source II (NSLS-II), a U.S. DOE Office of Science User Facility operated for the DOE Office of Science by Brookhaven National Laboratory (BNL) under contract no. DE-SC0012704. This material is based upon work supported by the National Science Foundation under grant no. 1762657.

# 7. Declaration of competing interests

The authors declare that they have no known competing financial interests or personal relationships that could have appeared to influence the work reported in this paper.

#### References

- N. Chawla, J. Jones, C. Andres, J. Allison, Effect of SiC volume fraction and particle size on the fatigue resistance of a 2080 Al/SiC<sub>p</sub> composite, Metallurgical and Materials Transactions A 29 (1998) 2843–2854.
- [2] S. Tjong, Z. Ma, Microstructural and mechanical characteristics of in situ metal matrix composites, Materials Science and Engineering: R: Reports 29 (3-4) (2000) 49–113.
- [3] J. Liu, X. Huang, K. Zhao, Z. Zhu, X. Zhu, L. An, Effect of reinforcement particle size on quasistatic and dynamic mechanical properties of Al-Al<sub>2</sub>O<sub>3</sub> composites, Journal of Alloys and Compounds 797 (2019) 1367–1371.
- [4] J. Hashim, L. Looney, M. Hashmi, The wettability of SiC particles by molten aluminium alloy, Journal of Materials Processing Technology 119 (1-3) (2001) 324–328.

- [5] Z. Hu, M. Pozuelo, M. Sokoluk, S. Mathaudhu, C. Roach, X. Li, J.-M. Yang, Micro-mechanical properties of homogeneous-and inhomogeneous-structured pillars in Al–TiC nanocomposite: An in-situ study, Materials Science and Engineering: A 762 (2019) 138084.
- [6] A. Kumar, P. Kumar, A review on the mechanical properties, tribological behavior and the microstructural characterization of aluminium metal matrix composites (ammcs), Int J Sci Eng Res 6 (6) (2015) 1234–1245.
- [7] W. Zhai, W. Zhou, S. M. L. Nai, Grain refinement and strengthening of 316L stainless steel through addition of TiC nanoparticles and selective laser melting, Materials Science and Engineering: A 832 (2022) 142460.
- [8] A. Wagih, A. Fathy, D. Ibrahim, O. Elkady, M. Hassan, Experimental investigation on strengthening mechanisms in Al-SiC nanocomposites and 3D FE simulation of Vickers indentation, Journal of Alloys and Compounds 752 (2018) 137–147.
- [9] J. Qin, G. Chen, B. Wang, N. Hu, F. Han, Z. Du, Formation of in-situ Al<sub>3</sub>Ti particles from globular Ti powders and Al alloy melt under ultrasonic vibration, Journal of Alloys and Compounds 653 (2015) 32–38.
- [10] Z. Liu, N. Cheng, Q. Zheng, J. Wu, Q. Han, Z. Huang, J. Xing, Y. Li, Y. Gao, Processing and tensile properties of A356 composites containing in situ small-sized Al<sub>3</sub>Ti particulates, Materials Science and Engineering: A 710 (2018) 392–399.
- [11] Z. Liu, Q. Han, J. Li, Formation of small blocky Al<sub>3</sub>Ti particles via direct reaction between solid Ti powders and liquid Al, Metallurgical and Materials Transactions A 43 (2012) 4460–4463.
- [12] S. C. Tjong, Novel nanoparticle-reinforced metal matrix composites with enhanced mechanical properties, Advanced engineering materials 9 (8) (2007) 639–652.
- [13] N. Chawla, K. K. Chawla, Processing, Metal matrix composites (2013) 55–97.
- [14] P. Li, E. Kandalova, V. Nikitin, A. Makarenko, A. Luts, Z. Yanfei, Preparation of Al–TiC composites by self-propagating high-temperature synthesis, Scripta materialia 49 (7) (2003) 699–703.
- [15] L. Ceschini, A. Dahle, M. Gupta, A. E. W. Jarfors, S. Jayalakshmi, A. Morri, F. Rotundo, S. Toschi, R. A. Singh, Aluminum and magnesium metal matrix nanocomposites, Springer, 2017.
- [16] Q. Guo, Y. Han, D. Zhang, Interface-dominated mechanical behavior in advanced metal matrix composites, Nano Materials Science 2 (1) (2020) 66–71.
- [17] I. Ibrahim, F. Mohamed, E. Lavernia, Particulate reinforced metal matrix composites—a review, Journal of materials science 26 (1991) 1137–1156.

- [18] B. Daniel, V. Murthy, G. Murty, Metal-ceramic composites via in-situ methods, Journal of Materials Processing Technology 68 (2) (1997) 132–155.
- [19] C. Reese, A. Gladstein, P. Shevchenko, X. Xiao, A. Shahani, A. Taub, Real-time visualization of particle evolution during reactive flux-assisted processing of aluminum melts, Scripta Materialia 201 (2021) 113978.
- [20] C. Reese, A. Gladstein, J. Fedors, V. De Andrade, B. Mishra, A. Shahani, A. Taub, In situ Al-TiC composites fabricated by self-propagating high-temperature reaction: Insights on reaction pathways and their microstructural signatures, Metallurgical and Materials Transactions A 51 (2020) 3587–3600.
- [21] S. Chatterjee, A. Ghosh, A. B. Mallick, Understanding the evolution of microstructural features in the in-situ intermetallic phase reinforced Al/Al<sub>3</sub>Ti nanocomposite, Materials Today: Proceedings 5 (3) (2018) 10118–10130.
- [22] I. Anza, M. M. Mahklouf, Synthesis of Al-TiC nanocomposites by an in-situ gas-liquid method, Light Metals 2016 (2016) 245–254.
- [23] I. Anza, M. M. Makhlouf, Synthesis of aluminum-titanium carbide micro and nanocomposites by the rotating impeller in-situ gas-liquid reaction method, Metallurgical and Materials Transactions B 49 (2018) 466–480.
- [24] H. Ding, W. Miao, W. Chu, Q. Liu, J. Wang, K. Chu, N. Glandut, C. Li, The reaction pathway of Ti-SiC system in Cu melts, Journal of Alloys and Compounds 818 (2020) 152860.
- [25] Y. Birol, In situ synthesis of Al– $TiC_p$  composites by reacting  $K_2TiF_6$  and particulate graphite in molten aluminium, Journal of Alloys and Compounds 454 (1-2) (2008) 110–117.
- [26] C. Cao, H. Ling, N. Murali, X. Li, In-situ molten salt reaction and incorporation of small (10 nm) TiC nanoparticles into Al, Materialia 7 (2019) 100425.
- [27] X. Wang, A. Jha, R. Brydson, In situ fabrication of Al<sub>3</sub>Ti particle reinforced aluminium alloy metal-matrix composites, Materials Science and Engineering: A 364 (1-2) (2004) 339–345.
- [28] V. Auradi, S. Kori, Influence of reaction temperature for the manufacturing of Al–3Ti and Al–3B master alloys, Journal of Alloys and Compounds 453 (1-2) (2008) 147–156.
- [29] N. El-Mahallawy, M. A. Taha, A. E. Jarfors, H. Fredriksson, On the reaction between aluminium, K<sub>2</sub>TiF<sub>6</sub> and KBF<sub>4</sub>, Journal of alloys and compounds 292 (1-2) (1999) 221–229.
- [30] G.-R. Li, H.-M. Wang, Y.-T. Zhao, D.-B. Chen, C. Gang, X.-N. Cheng, Microstructure of in situ Al<sub>3</sub>Ti/6351Al composites fabricated with electromagnetic stirring and fluxes, Transactions of Nonferrous Metals Society of China 20 (4) (2010) 577–583.

- [31] M. Lee, B. Terry, Effects of processing parameters on aluminide morphology in aluminium grain refining master alloys, Materials science and technology 7 (7) (1991) 608–612.
- [32] Y. Birol, Analysis of the response to thermal exposure of Al/K<sub>2</sub>TiF<sub>6</sub> powder blends, Journal of alloys and compounds 478 (1-2) (2009) 265–268.
- [33] J. Fjellstedt, A. E. Jarfors, On the precipitation of TiB<sub>2</sub> in aluminum melts from the reaction with KBF<sub>4</sub> and K<sub>2</sub>TiF<sub>6</sub>, Materials Science and Engineering: A 413 (2005) 527–532.
- [34] Y. Birol, Effect of the salt addition practice on the grain refining efficiency of Al–Ti–B master alloys, Journal of Alloys and Compounds 420 (1-2) (2006) 207–212.
- [35] H. Ding, X. Liu, L. Yu, G. Zhao, The influence of forming processes on the distribution and morphologies of TiC in Al–Ti–C master alloys, Scripta materialia 57 (7) (2007) 575–578.
- [36] Y.-H. Cho, J.-M. Lee, S.-H. Kim, Al-TiC composites fabricated by a thermally activated reaction process in an Al melt using Al-Ti-C-CuO powder mixtures. part i: microstructural evolution and reaction mechanism, Metallurgical and Materials Transactions A 45 (2014) 5667–5678.
- [37] R. Daudin, S. Terzi, P. Lhuissier, J. Tamayo, M. Scheel, N. H. Babu, D. Eskin, L. Salvo, Particle-induced morphological modification of Al alloy equiaxed dendrites revealed by sub-second in situ microtomography, Acta Materialia 125 (2017) 303–310.
- [38] E. Guo, S. Shuai, D. Kazantsev, S. Karagadde, A. Phillion, T. Jing, W. Li, P. D. Lee, The influence of nanoparticles on dendritic grain growth in Mg alloys, Acta Materialia 152 (2018) 127–137.
- [39] E. Guo, A. Phillion, Z. Chen, H. Kang, T. Wang, P. D. Lee, In situ tomographic observation of dendritic growth in Mg/Al matrix composites, in: Light Metals 2019, Springer, 2019, pp. 1561–1567.
- [40] J. W. Pegues, M. A. Melia, M. A. Rodriguez, T. F. Babuska, B. Gould, N. Argibay, A. Greco, A. B. Kustas, In situ synchrotron x-ray imaging and mechanical properties characterization of additively manufactured high-entropy alloy composites, Journal of Alloys and Compounds 876 (2021) 159505.
- [41] S. Li, B. Cai, R. Duan, L. Tang, Z. Song, D. White, O. V. Magdysyuk, M. M. Attallah, Synchrotron characterisation of ultra-fine grain TiB<sub>2</sub>/Al-Cu composite fabricated by laser powder bed fusion, Acta Metallurgica Sinica (English Letters) 35 (2022) 78–92.
- [42] W. Mirihanage, W. Xu, J. Tamayo-Ariztondo, D. Eskin, M. Garcia-Fernandez, P. Srirangam, P. Lee, Synchrotron radiographic studies of ultrasonic melt processing of metal matrix nano composites, Materials Letters 164 (2016) 484–487.
- [43] M. Schöbel, G. Requena, G. Fiedler, D. Tolnai, S. Vaucher, H. Degischer, Void formation in metal matrix composites by solidification and shrinkage of an AlSi7 matrix between densely packed particles, Composites Part A: Applied Science and Manufacturing 66 (2014) 103–108.

- [44] C. Puncreobutr, A. B. Phillion, J. L. Fife, P. Rockett, A. P. Horsfield, P. D. Lee, In situ quantification of the nucleation and growth of Fe-rich intermetallics during Al alloy solidification, Acta Materialia 79 (2014) 292–303.
- [45] A. Bjurenstedt, D. Casari, S. Seifeddine, R. H. Mathiesen, A. K. Dahle, In-situ study of morphology and growth of primary  $\alpha$ -Al (femner) Si intermetallics in an Al-Si alloy, Acta Materialia 130 (2017) 1–9.
- [46] Z. Song, O. V. Magdysyuk, L. Tang, T. Sparks, B. Cai, Growth dynamics of faceted Al<sub>1</sub>3Fe<sub>4</sub> intermetallic revealed by high-speed synchrotron x-ray quantification, Journal of Alloys and Compounds 861 (2021) 158604.
- [47] Z. Song, O. V. Magdysyuk, T. Sparks, Y.-L. Chiu, B. Cai, Revealing growth mechanisms of faceted Al<sub>2</sub>Cu intermetallic compounds via high-speed synchrotron x-ray tomography, Acta Materialia 231 (2022) 117903.
- [48] A. J. Shahani, X. Xiao, P. W. Voorhees, The mechanism of eutectic growth in highly anisotropic materials, Nature Communications 7 (1) (2016) 12953.
- [49] S. Moniri, X. Xiao, A. J. Shahani, Singly-twinned growth of si crystals upon chemical modification, Physical Review Materials 4 (6) (2020) 063403.
- [50] P. J. Withers, T. L. Burnett, Rich multi-dimensional correlative imaging, in: IOP Conference Series: Materials Science and Engineering, Vol. 580, IOP Publishing, 2019, p. 012014.
- [51] T. Burnett, S. McDonald, A. Gholinia, R. Geurts, M. Janus, T. Slater, S. Haigh, C. Ornek, F. Almuaili, D. Engelberg, et al., Correlative tomography, Scientific reports 4 (1) (2014) 4711.
- [52] M. Ge, D. S. Coburn, E. Nazaretski, W. Xu, K. Gofron, H. Xu, Z. Yin, W.-K. Lee, One-minute nano-tomography using hard x-ray full-field transmission microscope, Applied Physics Letters 113 (8) (2018).
- [53] A. J. Shahani, X. Xiao, E. M. Lauridsen, P. W. Voorhees, Characterization of metals in four dimensions, Materials Research Letters 8 (12) (2020) 462–476.
- [54] W.-K. Lee, R. Reininger, W. Loo, R. Gambella, S. O'Hara, Y. S. Chu, Z. Zhong, J. Wang, FXI: A full-field imaging beamline at NSLS-II, in: X-Ray Nanoimaging: Instruments and Methods II, Vol. 9592, SPIE, 2015, pp. 6–12.
- [55] D. Gürsoy, F. De Carlo, X. Xiao, C. Jacobsen, TomoPy: a framework for the analysis of synchrotron tomographic data, Journal of synchrotron radiation 21 (5) (2014) 1188–1193.
- [56] N. T. Vo, R. C. Atwood, M. Drakopoulos, Superior techniques for eliminating ring artifacts in x-ray micro-tomography, Optics express 26 (22) (2018) 28396–28412.

- [57] B. A. Dowd, G. H. Campbell, R. B. Marr, V. V. Nagarkar, S. V. Tipnis, L. Axe, D. P. Siddons, Developments in synchrotron x-ray computed microtomography at the National Synchrotron Light Source, in: Developments in X-ray Tomography II, Vol. 3772, SPIE, 1999, pp. 224–236.
- [58] ASM alloy phase diagram database, https://matdata-asminternational-org.proxy.lib.umich.edu/apd/index.aspx (2022).
- [59] B. L. Henke, E. M. Gullikson, J. C. Davis, X-ray interactions: photoabsorption, scattering, transmission, and reflection at E=50-30,000 eV, Z=1-92, Atomic data and nuclear data tables 54 (2) (1993) 181–342.
- [60] P. Modregger, D. Lübbert, P. Schäfer, R. Köhler, Spatial resolution in bragg-magnified x-ray images as determined by fourier analysis, physica status solidi (a) 204 (8) (2007) 2746–2752.
- [61] A. J. Shahani, E. B. Gulsoy, J. W. Gibbs, J. L. Fife, P. W. Voorhees, Integrated approach to the data processing of four-dimensional datasets from phase-contrast x-ray tomography, Optics express 22 (20) (2014) 24606–24621.
- [62] R. Shi, J. M. Meier, A. A. Luo, Controlling particle/metal interactions in metal matrix composites during solidification: the role of melt viscosity and cooling rate, Metallurgical and Materials Transactions A 50 (2019) 3736–3747.
- [63] V. Auradi, S. Amarappa Kori, Effect of processing temperature on the microstructure of Al-7Ti master alloy and on refinement of α-Al dendrites in Al-7Si alloys, Advanced Materials Letters 6 (3) (2015) 252–259.
- [64] J. A. Dantzig, M. Rappaz, Solidification: Revised & Expanded, EPFL press, 2016.
- [65] R. F. Sekerka, Role of instabilities in determination of the shapes of growing crystals, Journal of crystal growth 128 (1-4) (1993) 1–12.
- [66] R. Sekerka, G. Müller, J. Métois, P. Rudolph, Crystal growth–from fundamentals to technology, editors, G. Müller, J.-J. Métois, P. Rudolph (2004) 55.
- [67] D. S. John, L. Hogan, Metallography and growth crystallography of Al<sub>3</sub>Ti in Al-Ti alloys up to 5 wt% Ti, Journal of Crystal Growth 46 (3) (1979) 387–398.
- [68] W. Ding, T. Xia, W. Zhao, Performance comparison of Al–Ti master alloys with different microstructures in grain refinement of commercial purity aluminum, Materials 7 (5) (2014) 3663–3676.
- [69] L. Arnberg, L. Bäckerud, H. Klang, 1: Production and properties of master alloys of Al–Ti–B type and their ability to grain refine aluminium, Metals Technology 9 (1) (1982) 1–6.

- [70] M. Yousefi, H. Doostmohammadi, R. Raiszadeh, The effect of melt composition and cooling rate on Al<sub>3</sub>Ti morphology in Al-Al<sub>3</sub>Ti composite, Advances in Metallurgical Prosses and Materials, Ukraine, Lviv (2018).
- [71] J. Zhao, T. Wang, J. Chen, L. Fu, J. He, Effect of cooling rate on morphology of TiAl<sub>3</sub> particles in Al–4Ti master alloy, Materials 10 (3) (2017) 238.
- [72] R. Ghomashchi, The evolution of AlTiSi intermetallic phases in Ti-added A356 Al–Si alloy, Journal of Alloys and Compounds 537 (2012) 255–260.
- [73] N. Blake, R. Smith, Preferred orientation of rapidly frozen metals, Canadian Journal of Physics 60 (12) (1982) 1720–1724.
- [74] A. Majumdar, B. Muddle, Microstructure in rapidly solidified Al-Ti alloys, Materials Science and Engineering: A 169 (1-2) (1993) 135–147.
- [75] K. Hyde, A. Norman, P. Prangnell, The effect of cooling rate on the morphology of primary Al<sub>3</sub>Sc intermetallic particles in Al–Sc alloys, Acta Materialia 49 (8) (2001) 1327–1337.
- [76] K. Yan, Z. Chen, Y. Zhao, C. Ren, W. Lu, A. Aldeen, Morphological characteristics of Al<sub>3</sub>Sc particles and crystallographic orientation relationships of Al<sub>3</sub>Sc/Al interface in cast Al-Sc alloy, Journal of Alloys and Compounds 861 (2021) 158491.
- [77] J. Zhao, J. He, Q. Tang, T. Wang, J. Chen, Grain refinement efficiency in commercial-purity aluminum influenced by the addition of Al-4Ti master alloys with varying TiAl<sub>3</sub> particles, Materials 9 (11) (2016) 869.
- [78] B. E. Sundquist, L. Mondolfo, Heterogeneous nucleation in the liquid-to-solid transformation in alloys, Transactions of the Metallurgical Society of AIME 221 (1) (1961) 157–164.
- [79] C. Lemaignan, Initial stages of eutectic solidification, Acta Metallurgica 29 (8) (1981) 1379–1384.
- [80] V. Podolinsky, Non-reciprocal heterogeneous nucleation in eutectic systems, Journal of crystal growth 98 (4) (1989) 838–842.
- [81] Y. Cui, D. King, A. Horsfield, C. Gourlay, Solidification orientation relationships between Al<sub>3</sub>Ti and TiB<sub>2</sub>, Acta Materialia 186 (2020) 149–161.
- [82] F. Wang, D. Eskin, J. Mi, T. Connolley, J. Lindsay, M. Mounib, A refining mechanism of primary Al<sub>3</sub>Ti intermetallic particles by ultrasonic treatment in the liquid state, Acta Materialia 116 (2016) 354–363.
- [83] S. Moniri, H. Bale, T. Volkenandt, Y. Wang, J. Gao, T. Lu, K. Sun, R. O. Ritchie, A. J. Shahani, Multi-step crystallization of self-organized spiral eutectics, Small 16 (8) (2020) 1906146.

- [84] M. J. Buerger, Elementary crystallography, John Wiley & Sons, 1956.
- [85] H. Sato, Y. Watanabe, Three-dimensional microstructural analysis of fragmentation behavior of platelet Al<sub>3</sub>Ti particles in Al-Al<sub>3</sub>Ti composite deformed by equal-channel angular pressing, Materials Characterization 144 (2018) 305–315.
- [86] M. Yamaguchi, Y. Umakoshi, T. Yamane, Plastic deformation of the intermetallic compound Al<sub>3</sub>Ti, Philosophical Magazine A 55 (3) (1987) 301–315.
- [87] R. M. German, P. Suri, S. J. Park, Liquid phase sintering, Journal of materials science 44 (2009) 1–39.
- [88] J. W. Cahn, J. E. Taylor, A unified approach to motion of grain boundaries, relative tangential translation along grain boundaries, and grain rotation, Acta Materialia 52 (16) (2004) 4887–4898.
- [89] M. Ebner, F. Marone, M. Stampanoni, V. Wood, Visualization and quantification of electrochemical and mechanical degradation in Li ion batteries, Science 342 (6159) (2013) 716–720.
- [90] J. C. Schuster, H. Ipser, Phases and phase relations in the partial system TiAl<sub>3</sub>-TiAl / phasen und phasenbeziehungen im teilbereich TiAl<sub>3</sub>-TiAl, International Journal of Materials Research 81 (6) (1990) 389–396.
- [91] T. Sun, W. Xu, X. Wu, Y. Jiang, X. Qu, Structural and mechanical properties of Al/TiC interface with vacancies: First-principles study, Physics Letters A 471 (2023) 128786.
- [92] S. Reavley, A. Greer, Athermal heterogeneous nucleation of freezing: numerical modelling for polygonal and polyhedral substrates, Philosophical Magazine 88 (4) (2008) 561–579.
- [93] A. Greer, A. Bunn, A. Tronche, P. Evans, D. Bristow, Modelling of inoculation of metallic melts: application to grain refinement of aluminium by Al–Ti–B, Acta materialia 48 (11) (2000) 2823–2835.
- [94] T. Fujinaga, Y. Shibuta, Molecular dynamics simulation of athermal heterogeneous nucleation of solidification, Computational Materials Science 164 (2019) 74–81.
- [95] D. Wearing, A. P. Horsfield, W. Xu, P. D. Lee, Which wets TiB<sub>2</sub> inoculant particles: Al or Al<sub>3</sub>Ti?, Journal of Alloys and Compounds 664 (2016) 460–468.
- [96] G. I. Tóth, G. Tegze, T. Pusztai, L. Gránásy, Heterogeneous crystal nucleation: the effect of lattice mismatch, Physical review letters 108 (2) (2012) 025502.
- [97] L. Yu, X. Liu, Ti transition zone on the interface between TiC and aluminum melt and its influence on melt viscosity, Journal of materials processing technology 182 (1-3) (2007) 519–524.
- [98] J. Sekhar, R. Trivedi, Solidification microstructure evolution in the presence of inert particles, Materials Science and Engineering: A 147 (1) (1991) 9–21.

- [99] R. Folch, M. Plapp, Quantitative phase-field modeling of two-phase growth, Physical Review E 72 (1) (2005) 011602.
- [100] D. Fan, L.-Q. Chen, Computer simulation of grain growth using a continuum field model, Acta Materialia 45 (2) (1997) 611–622.
- [101] N. Ofori-Opoku, N. Provatas, A quantitative multi-phase field model of polycrystalline alloy solidification, Acta Materialia 58 (6) (2010) 2155–2164.
- [102] H.-C. Yu, H.-Y. Chen, K. Thornton, Extended smoothed boundary method for solving partial differential equations with general boundary conditions on complex boundaries, Modelling and Simulation in Materials Science and Engineering 20 (7) (2012) 075008.
- [103] S. DeWitt, S. Rudraraju, D. Montiel, W. B. Andrews, K. Thornton, Prisms-pf: A general framework for phase-field modeling with a matrix-free finite element method, npj Computational Materials 6 (1) (2020) 29.
- [104] L. Aagesen, J. Adams, J. Allison, W. Andrews, V. Araullo-Peters, T. Berman, Z. Chen, S. Daly, S. Das, S. DeWitt, et al., Prisms: An integrated, open-source framework for accelerating predictive structural materials science, JOM 70 (2018) 2298–2314.
- [105] L. Svendsen, A. Jarfors, Al–Ti–C phase diagram, Materials science and technology 9 (11) (1993) 948–957.
- [106] R. Mitra, M. Fine, J. Weertman, Chemical reaction strengthening of Al/TiC metal matrix composites by isothermal heat treatment at 913 K, Journal of materials research 8 (9) (1993) 2370–2379.
- [107] N. Frage, M. Polak, M. Dariel, N. Frumin, L. Levin, High-temperature phase equilibria in the Al-rich corner of the Al-Ti-C system, Metallurgical and Materials Transactions A 29 (1998) 1341–1345.
- [108] Y. Ye, P. Li, L. He, Valence electron structure analysis of morphologies of Al<sub>3</sub>Ti and Al<sub>3</sub>Sc in aluminum alloys, Intermetallics 18 (2) (2010) 292–297.
- [109] B. L. Bramfitt, The effect of carbide and nitride additions on the heterogeneous nucleation behavior of liquid iron, Metallurgical Transactions 1 (1970) 1987–1995.
- [110] M. Johnson, L. Eriksson, Thermal expansion of Al and TiB<sub>2</sub> in the temperature range 300 to 900 K and calculated lattice fit at the melting temperature for Al, International Journal of Materials Research 89 (7) (2021) 478–480.

# **Figures**

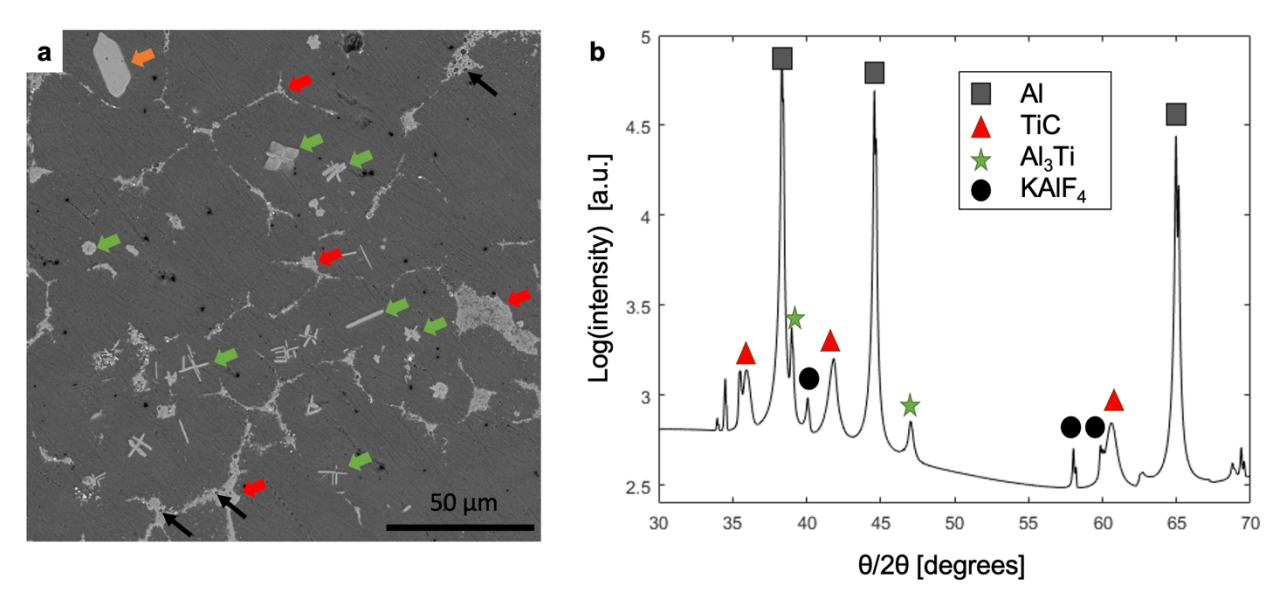


**Fig. 1:** Microstructure of quenched Al-TiC MMNC. (a) Representative SEM micrograph. TiC (red arrows) and Al<sub>3</sub>Ti (green and orange arrows) are both present. Black arrows point to residual flux. (b) XRD pattern of the as-made material. Peaks for Al, TiC, Al<sub>3</sub>Ti and KAlF<sub>4</sub> are indicated.

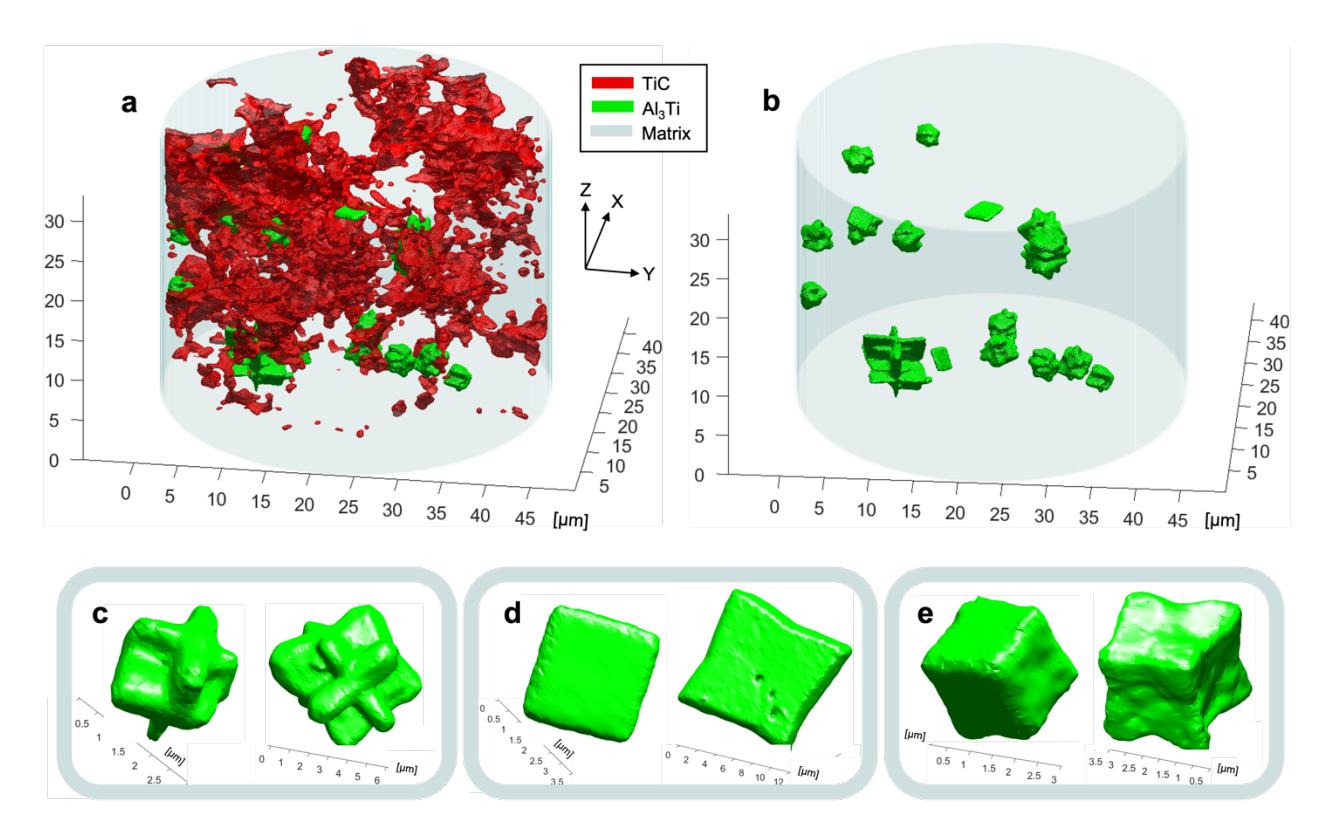


**Fig. 2:** Nanoscopic visualization via synchrotron TXM, showing (a) a cylindrical section of a micropillar sample (translucent blue) that contains Al<sub>3</sub>Ti particles (green) and TiC agglomerates (red). (b) Same volume rendering as in (a), but now displaying only Al<sub>3</sub>Ti for clarity. (c-e) Magnified views of three types of Al<sub>3</sub>Ti intermetallics: (c) "orthogonal plates," (d) "individual plates," and (e) cuboidal structures. Two examples are given of each, where the only difference between the left and right structure is the length-scale. The larger Al<sub>3</sub>Ti intermetallics at right in (c-e) have sides that have been bowed out likely due to a corner instability in solidification.

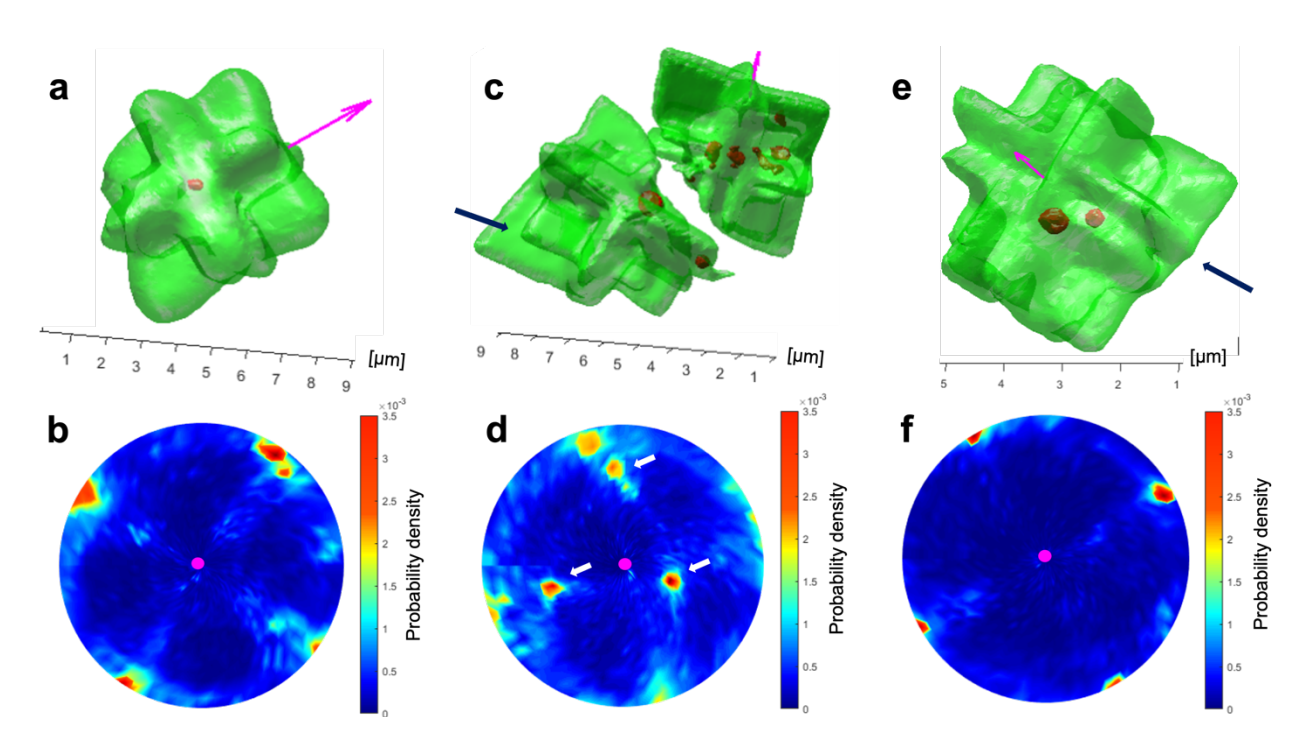


**Fig. 3:** Directionality of orthogonal plates. (top row) 3D snapshots of (a)  $Al_3Ti$  intermetallic (translucent green) with TiC particle (red) in its center, (c) two misaligned  $Al_3Ti$  intermetallics each containing a TiC particle, and (e)  $Al_3Ti$  intermetallic with two TiC particles and two sets of orthogonal plates. The latter was likely born from two separate intermetallics that later coalesced in solidification. (bottom row: b, d, f) Interfacial normal distributions corresponding to the same structures in (a, c, e), respectively, where the zone axis is taken as the pink arrow in each. White arrows in (d) point to facets of the misaligned intermetallic (at left in c). Extra plates in (c,e) indicated by blue arrows. See text for details.

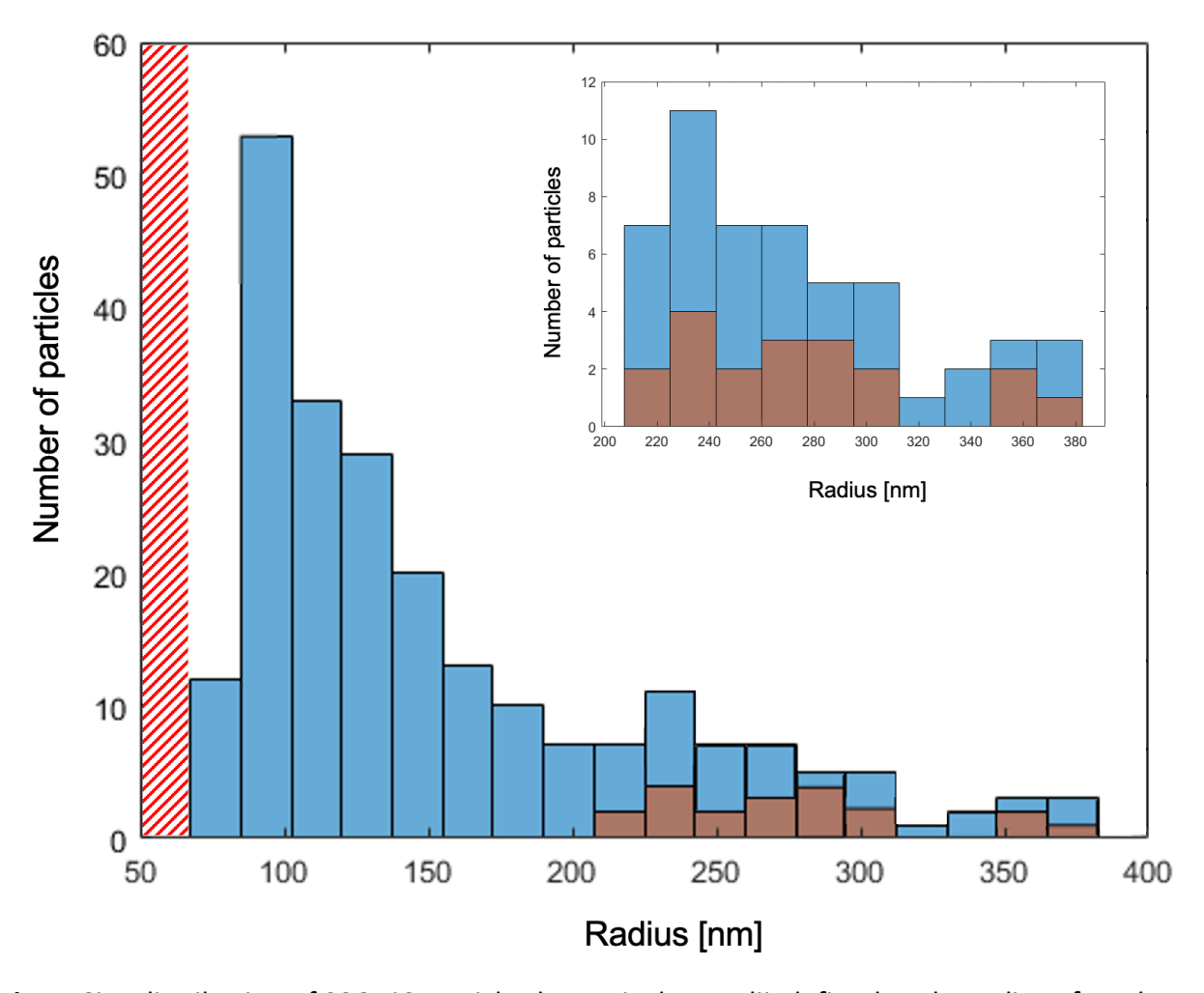


**Fig. 4.** Size distribution of 236 TiC particles by equivalent radii, defined as the radius of a sphere having the same volume as the particle (in 3D). Orange bins are associated with those TiC particles that are embedded within the orthogonal plates of Al<sub>3</sub>Ti (see Fig. 3(a)). The minimum radius reported here (60 nm, corresponding to the left-most edge of the histogram) is greater than the measured spatial resolution of TXM (50 nm, see the Supplementary Information) while the maximum was chosen to avoid counting agglomerates of TiC. That is, particles within the red-hatched area may not be observable using TXM due to resolution limitations. Inset is a magnified view, focusing on the radius-range covered by the embedded TiC. Meanwhile, TiC particles to the right of the hatched area are not generally embedded within the orthogonal plates of Al<sub>3</sub>Ti (unless they are of the size indicated by the orange bins).

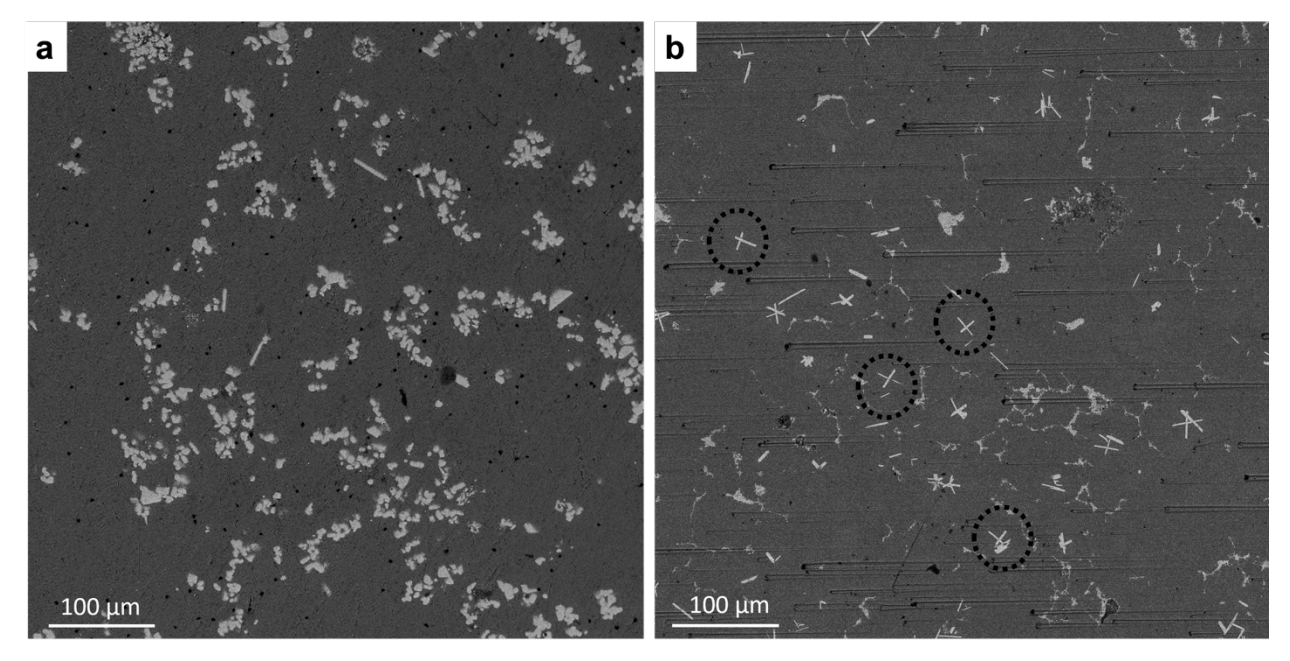


**Fig. 5:** Morphologies of  $Al_3Ti$  with and without inoculation: (a) an alloy prepared utilizing flux to form  $Al_3Ti$ , quenched using a copper plate, and without the addition of carbon to form TiC; (b) identical material processed under the same conditions but including TiC. We observe the formation of orthogonal plates in the presence of TiC (see black-circled regions in (b)).

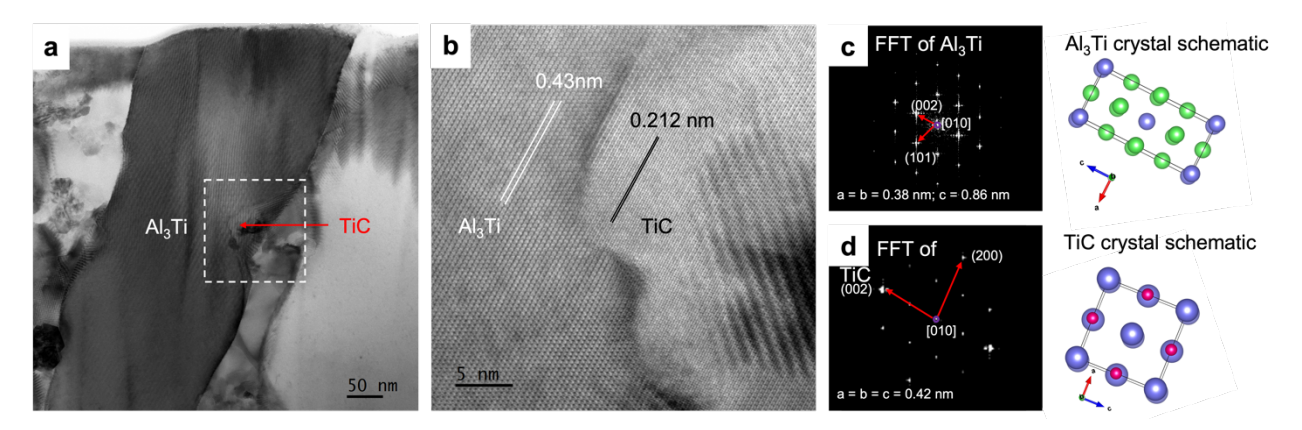


**Fig. 6:** Interface between nanoparticle and intermetallic. (a) Low magnification HAADF STEM image. (b) High resolution STEM micrograph (boxed region in a), showing the epitaxial relationship between Al₃Ti and TiC. (c-d) FFT patterns from (b), with schematics of the Al₃Ti crystal along [010] beam direction and TiC crystal along [010].

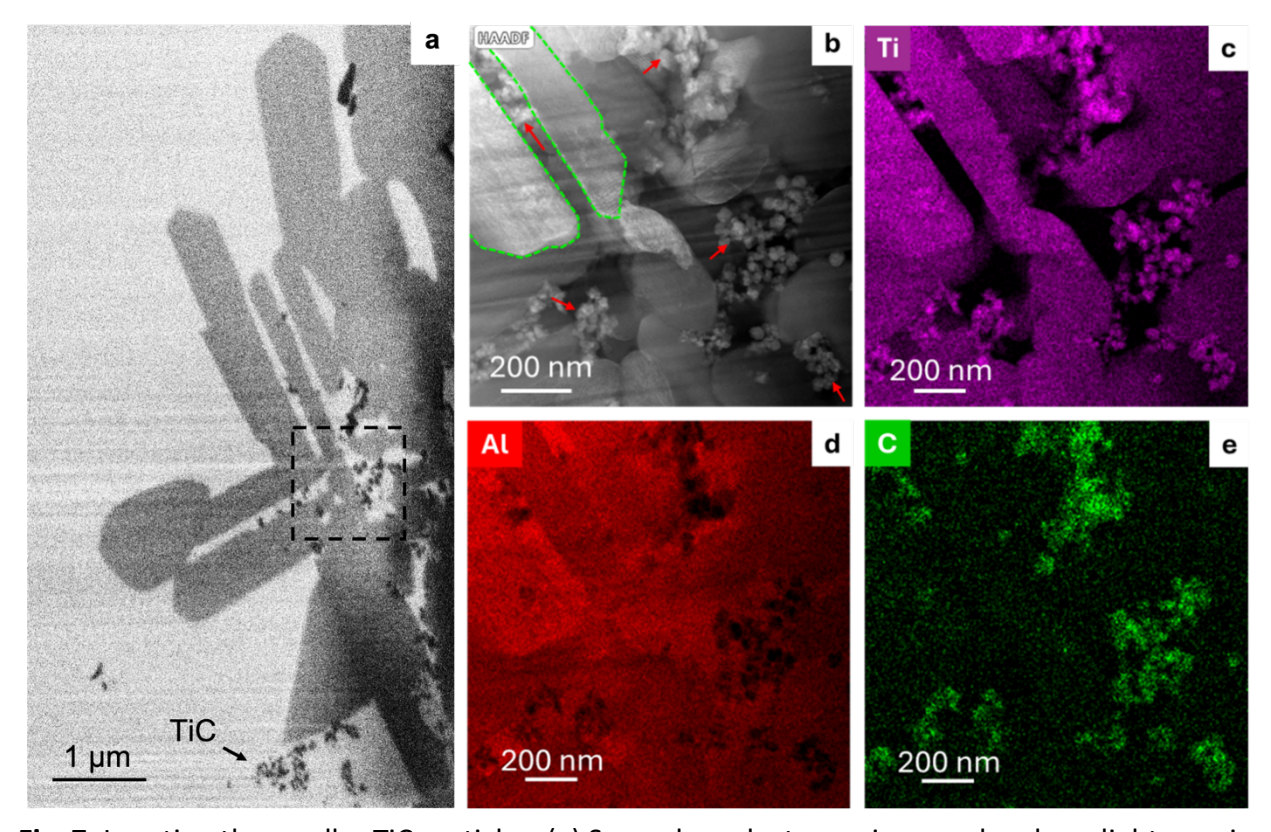


**Fig. 7:** Locating the smaller TiC particles. (a) Secondary electron micrograph, where light gray is the Al matrix, dark gray is Al $_3$ Ti, and black specks are TiC. (b) HAADF imaging of the boxed region in (a). The green outline in (b) highlights some of the parallel plates of Al $_3$ Ti. Red arrows point to TiC particles that lie outside of the Al $_3$ Ti intermetallic structure (see, *e.g.*, the top left red arrow). (c-e) Ti, Al, and C spectra for the region-of-interest shown in (b), respectively, showing a strong Ti signal in both Al $_3$ Ti and TiC phases.

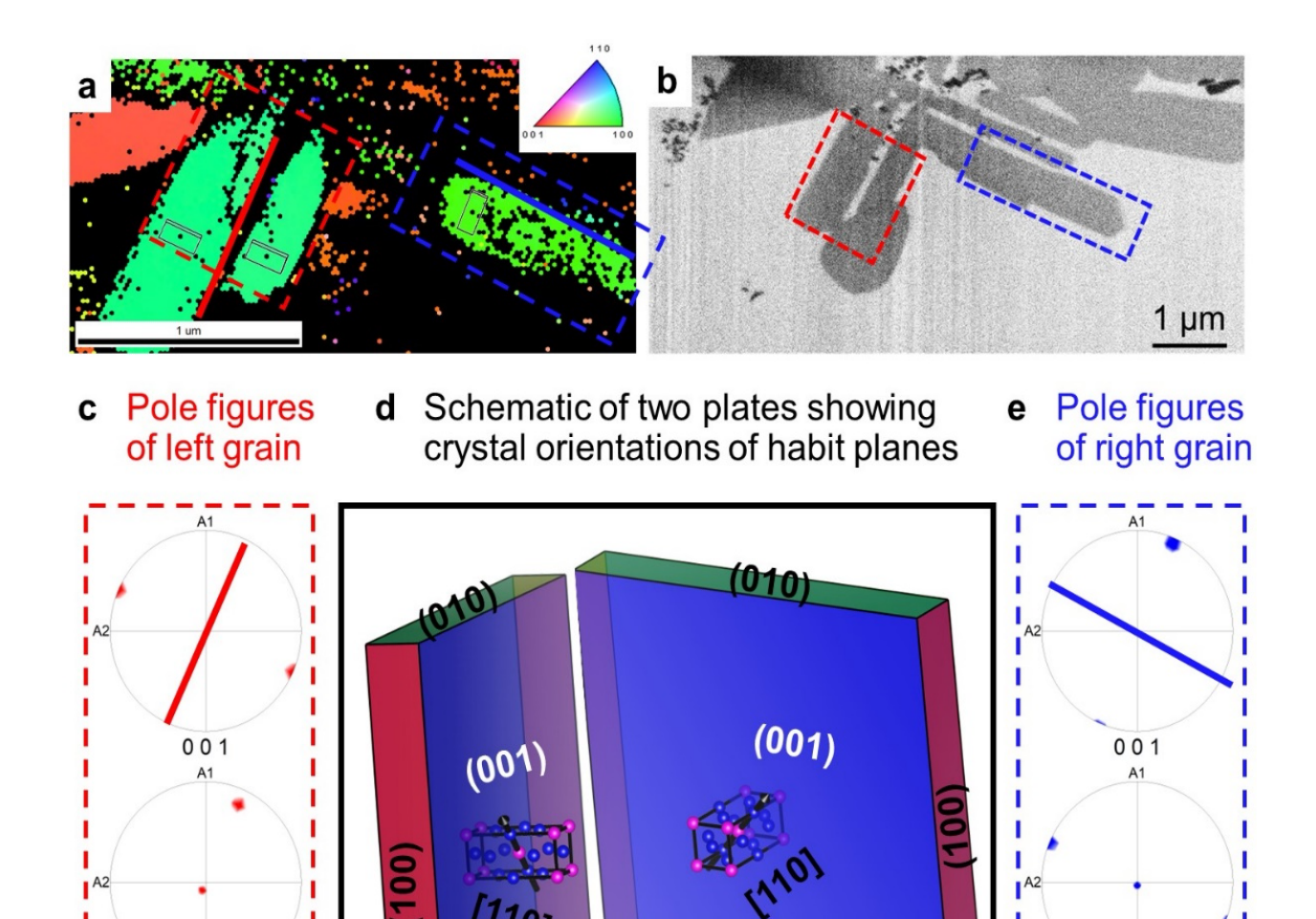


**Fig. 8:** (a) Inverse pole figure map corresponding to the morphology depicted in (b), obtained using TKD. Pole figures for the left grain are displayed in (c) (highlighted by a red box), while those for the right grains are shown in (e) (highlighted by a blue box). Data from both grains determines the orientations of the 3D plates as depicted schematically in (d).

100

110

-

-

100

110

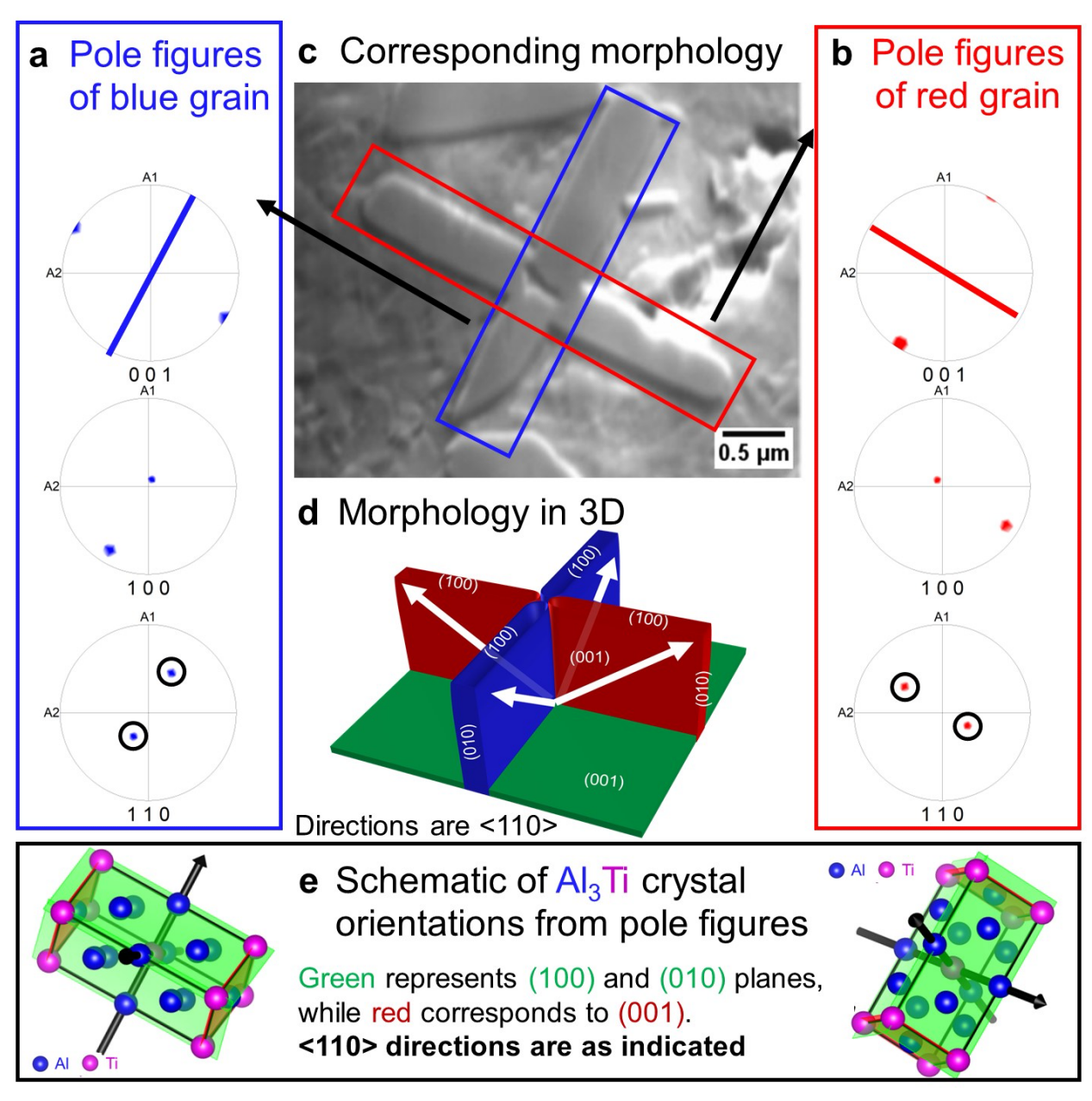


**Fig. 9:** (a-b) pole figures corresponding to the blue and red highlighted regions, respectively, of the orthogonal plate structure in (c). The observed orientations have been conveyed on an illustration of the 3D structure in (d). Crystal schematics corresponding to (a-b) are shown in (e).

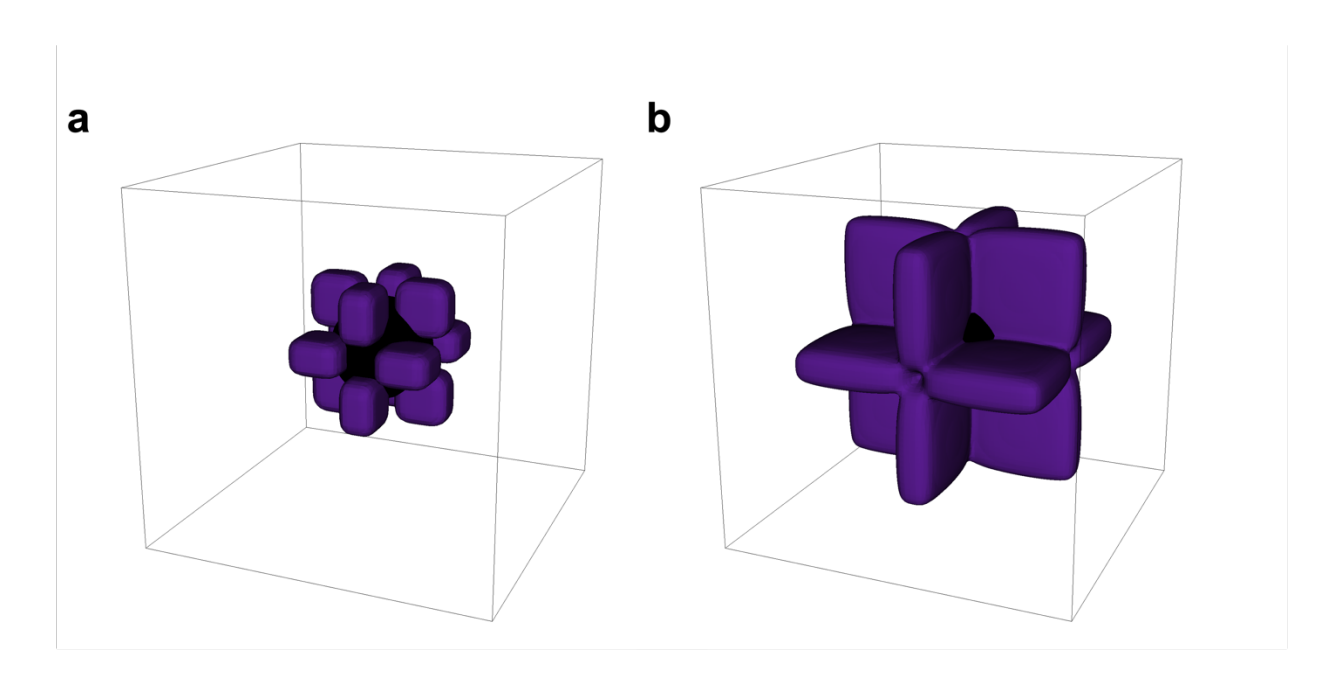


**Fig. 10:** Morphologies of Al<sub>3</sub>Ti grains in an orthogonal configuration: (a) the initial condition and (b) at simulation time of 0.2185 s. The box shown in the figure is  $2.5~\mu m \times 2.5~\mu m \times 2.5~\mu m$  in size.

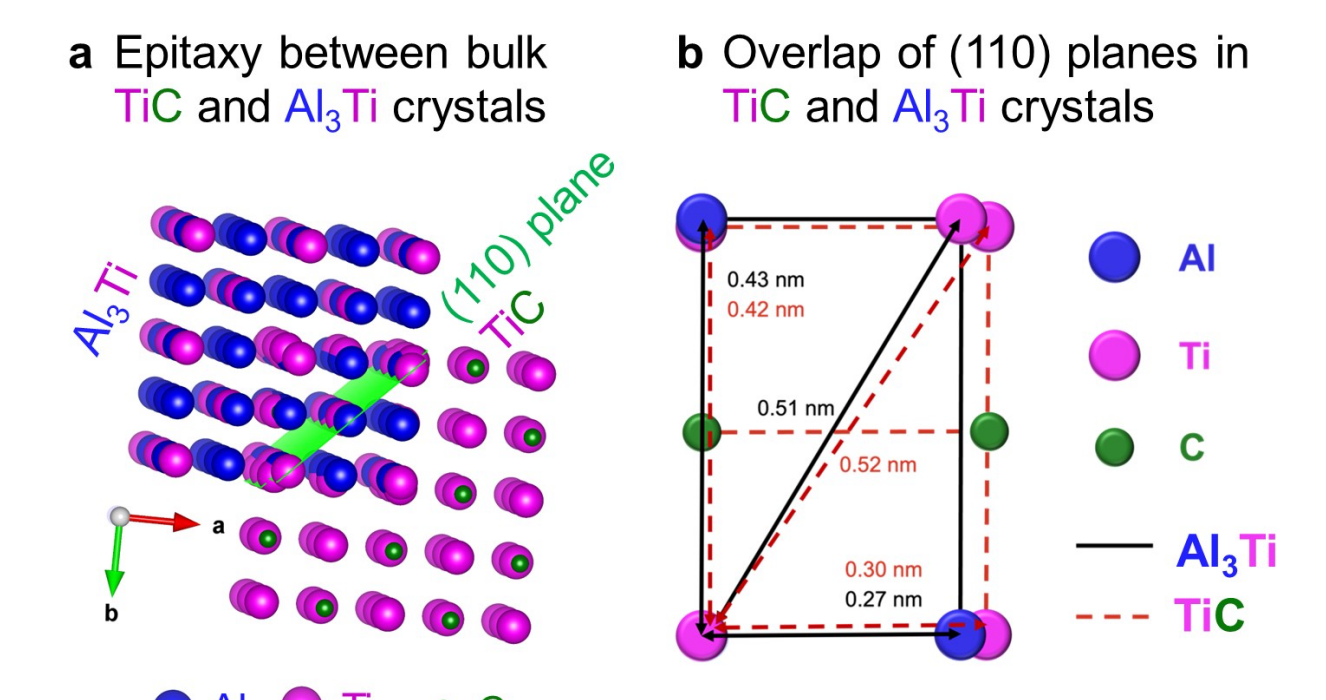
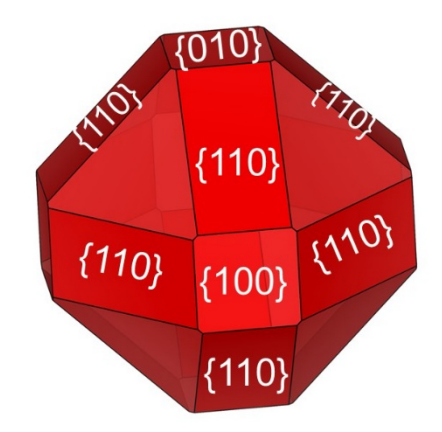
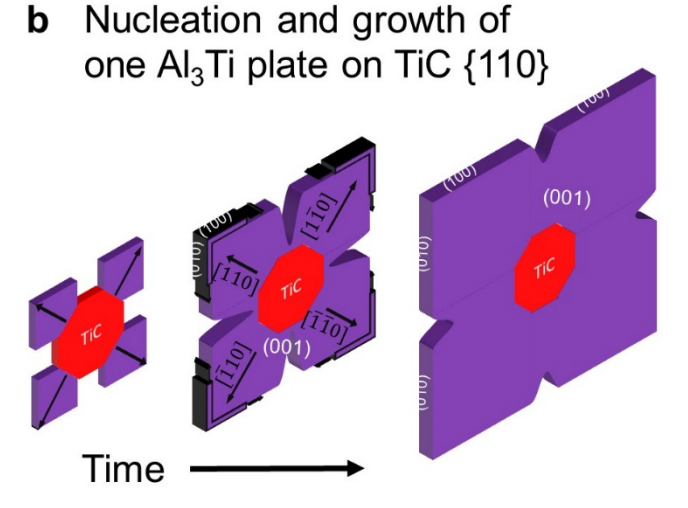


**Fig. 11:** (a) Illustration of epitaxy between TiC and Al<sub>3</sub>Ti, where the light green surface indicates the common plane (110). (b) Overlay of (110) crystallographic planes of Al<sub>3</sub>Ti and TiC, in which the Al<sub>3</sub>Ti plane is represented by black solid lines with blue and magenta circles denoting Al atoms and Ti atoms, respectively, and the TiC plane is noted with dashed red lines with magenta circles for Ti atoms and green circles for C atoms. Fig. (b) provides the three sets of interatomic spacing values used in the calculation of the disregistry level. See text for details.

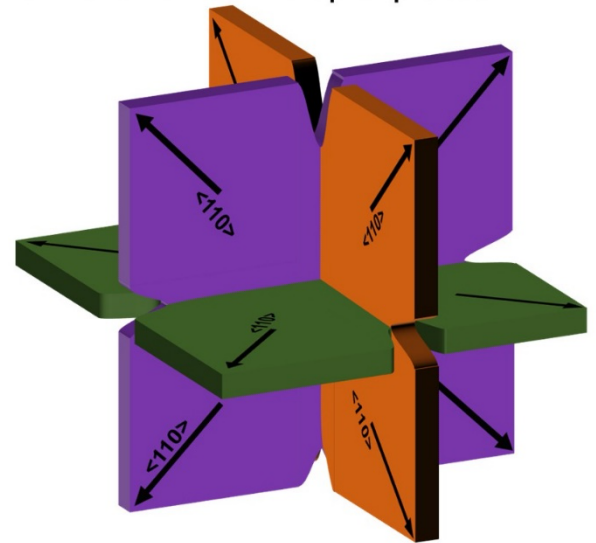
**a** {100}, {110}, {111} planes of TiC nucleant particle



c Growth of multiple plates



**d** SEM image of etched specimen



Arrows indicate <110> Al<sub>3</sub>Ti Three colors show three grains

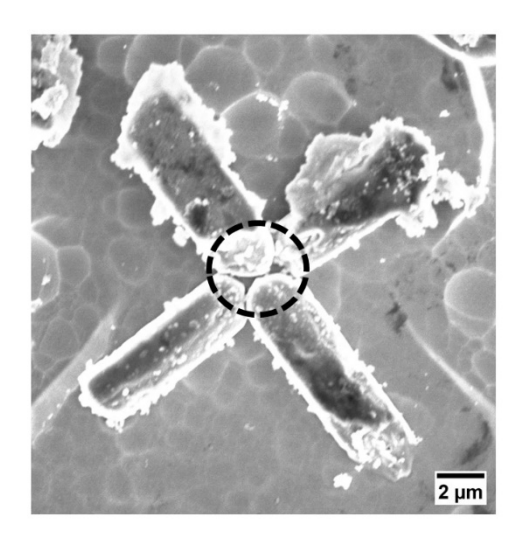


**Fig. 12:** (a) Depiction of  $\{100\}$ ,  $\{110\}$ , and  $\{111\}$  planes within the TiC crystal. (b) Visualization of the nucleation and growth of four Al<sub>3</sub>Ti crystals on four out of 12  $\{110\}$  TiC planes, corresponding to one of the three orthogonal grains. (c) Growth of all three grains, where the three colors correspond to their three unique orientations (see also Figs. 8-9). (d) SEM image displaying orthogonal structure in an etched specimen, showing gaps between the individual plates (see circled region), *cf.* Figs. (b-c).